TOPICAL REVIEW

A review on cathode materials for advanced lithium ion batteries: microstructure designs and performance regulations

To cite this article: Zhangxian Chen *et al* 2020 *Nanotechnology* **31** 012001

View the article online for updates and enhancements.

IOP ebooks™

Bringing you innovative digital publishing with leading voices to create your essential collection of books in STEM research.

Start exploring the collection - download the first chapter of every title for free.

Topical Review

A review on cathode materials for advanced lithium ion batteries: microstructure designs and performance regulations

Zhangxian Chen[1,2]**, Weixin Zhang**[1] **and Zeheng Yang**[1]

[1] School of Chemistry & Chemical Engineering, Hefei University of Technology, Hefei 230009, People's Republic of China
[2] School of Materials Science & Engineering, Hefei University of Technology, Hefei 230009, People's Republic of China

E-mail: wxzhang@hfut.edu.cn

Abstract

To meet the demands in portable electronic devices, electric vehicles and stationary energy storage, it is necessary to prepare advanced lithium ion batteries (LIBs) with high energy density and fast charge and discharge capabilities. Cathode materials, which account for 40%–50% of the cost of a whole battery, play a decisive role in cell voltage and capacity. Moreover, the performances of the cathodes are also balanced by many other aspects, including cycle life, rate capability, safety, costs, and environmental benignity. Unfortunately, none of the currently available cathode materials (e.g. $LiFePO_4$, $LiNi_xCo_yMn_{1-x-y}O_2$ layered oxides and Li-rich layered oxides) can get all the quests in a single cell. The electrochemical performances of a cathode are closely connected with its structural features, such as the porosities, morphologies and specifically exposed surfaces, which can be tuned by delicate designs. Here, we review our work on the rational design and delicate preparation of a series of cathode materials with controllable microstructures. We reveal the synergistic effects of both reaction and mass transfer on the formation of these meso-scale structures and the improved electrochemical performances of the cathode materials. The review will provide a scientific basis for the large-scale production of meso-scale structured cathode materials, and lay theoretical and experimental foundation for the application of cathode materials in next-generation LIBs.

Keywords: lithium ion battery, microstructure design, performance regulation, kinetically controlled synthesis, cathode materials

(Some figures may appear in colour only in the online journal)

1. Introduction

The ever-increasing concerns on the consumption of fossil fuels and environmental crisis have driven us to develop renewable energy and energy storage devices. As an important energy storage device with the advantages of light weight and high energy density, lithium ion batteries (LIBs) are increasingly reshaping our daily life [1]. LIBs are nowadays widely used to power our portable electronics (e.g. mobile phones, digital cameras and laptops) and electric vehicles (EVs) [2, 3].

The working principle of a single LIB cell is shown in figure 1, which consists of a cathode, an anode, a micro-porous polymer separator in between to prevent short circuit and a Li^+-containing electrolyte dissolved in organic solvents [1]. During discharging state, lithium ions are extracted from the anode, passing through the separator and finally intercalated into the cathode. An external current is thus obtained to drive our electrical apparatus. The process occurs spontaneously due to the favorable thermodynamics of the reaction. While during charging state, an external voltage is essential to drive the reversed
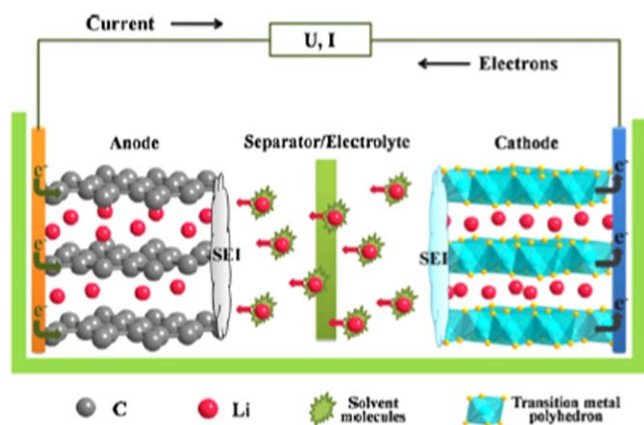
Figure 1. The working principle of a single LIB cell (charging). Reprinted from [1], Copyright 2012, with permission from Elsevier.

thermodynamically-uphill reaction. Lithium ions shuttle between the two active electrodes in a rocking-chair manner.

To satisfy our endless desires for long usage time of portable electronics and long driving range of EVs, advanced LIBs with improved energy density are essential. Graphite is currently the most promising anode material, due to its highly reversible lithiation/delithiation reactions and low lithiation potential [4]. Compared with the high capacity of the currently used graphite anode (Theoretical capacity of 372 mAh g^{-1}), the relatively low capacity of cathodes (generally <200 mAh g^{-1} when considering a decent cycling capability) has become the bottleneck for the improvement of LIB energy density [1, 3]. In addition, other key performances of LIBs, including the rate capability and cycle life, are also determined by the intrinsic chemistry of the cathode materials [3]. For example, the rate capability is highly related to the electronic and ionic conductivities of the cathode materials.

Layered LiCoO$_2$ cathode material has been mainly used in portable electronics, since its first demonstration for LIB in 1980 [5]. However, the energy density of LiCoO$_2$ cathode is relatively low for other applications, such as EVs and stationary energy storage, due to its low capacity (up to 160 mAh g^{-1}). Therefore, a material evolution of LIB cathode is deemed crucial to enhance the energy density of advanced LIBs by searching for novel cathode materials with either larger capacity or higher operating voltage [6, 7]. The cathode materials have evolved from LiCoO$_2$ to many other categorizes, including olivine LiFePO$_4$, spinel LiM$_2$O$_4$ (M =Ni, Mn, etc), layered compounds of LiMO$_2$ (M = Ni, Co, Mn, etc) and lithium-rich layered oxide xLi$_2$MnO$_3$(1−x)LiMO$_2$ (M = Ni, Co, Mn, etc). These cathode compounds are advantageous in energy density due to their higher operating voltage or larger discharge capacity. For example, the voltage plateau for LiNi$_{0.5}$Mn$_{1.5}$O$_4$ is as high as 4.7 V versus Li$^+$/Li [6, 8]. Ni-rich layered LiMO$_2$ (M = Ni, Co, Mn, etc) cathode could have the discharge capacity around 200 mAh g^{-1} [7, 9]. Especially, lithium-rich layered oxide xLi$_2$MnO$_3$(1−x)LiMO$_2$ (M = Ni, Co, Mn, etc) has extremely high capacity over 250 mAh g^{-1} [7, 10]. In addition, they share the same benefit of lower cost due to the reduced content or even no usage of Co, compared with LiCoO$_2$.

Bear in mind, the performances of cathodes are also balanced by many other aspects, including cycle life, rate capability, safety and environmental benignity. Unfortunately, none of the currently available cathode materials can get all the quests in a single cell, due to the problems intrinsically associated. For instance, Ni^{2+}/Li$^+$ mixing is common in layered LiMO$_2$ (M = Ni, Co, Mn, etc) due to their close ionic radii. The higher the nickel content, the severer the cationic mixing, which thus makes Ni-rich layered LiMO$_2$ face the common problem of short cycle life. Therefore, for a given cathode material, the intriguing thing is how to rationally design its microstructure, to push the capacity to the limit and to solve one or more of its problems as an add-up.

The microstructures of cathodes could have a pivotal role on their performances in LIBs, which include the morphologies, porosities, surface chemistries, etc [11]. For instance, the diffusion time of Li$^+$ (τ) through an electrode material can be estimated as: $\tau \propto l^2/D$, where l and D refer to the diffusion length and coefficient, respectively. A porous cathode material can provide better contact between the electrolyte and cathode surface than the bulk. The thin walls of the porous cathode can effectively reduce the diffusion path of Li$^+$. As a result, the rate capability of the LIBs can be greatly improved [12].

Another example is the crystal face tuning of Li[Li$_{1/3−2x/3}$Ni$_x$Mn$_{2/3−x/3}$]O$_2$ cathode reported by Sun's group [13]. Due to the crystal anisotropic feature of this α-NaFeO$_2$-type cathode, the diffusion of Li$^+$ cations along the (001) plane is much slower than along other planes, such as (010). The (010)-dominated Li[Li$_{1/3−2x/3}$Ni$_x$Mn$_{2/3−x/3}$]O$_2$ nanoplate cathode displayed significantly enhanced rate performance of 186 mAh g^{-1} after 50 cycles at 6 C rate than the (001)-dominated counterpart (only 106 mAh g^{-1}). However, the synthesis of these microstructural features requires a rational design. Even a kinetic control to break the thermodynamically favorable growth condition is essential [13].

In this topical review, we will summarize our rational designs of composition and microstructure for variety of cathode materials to achieve their high energy density, with the material compositions varying from olive-type LiFePO$_4$, to high voltage spinel LiMn$_2$O$_4$, and to the high capacity layered oxides. We wish to demonstrate the basic synthesis chemistry of each category and our rational designs to synthesize these cathode materials with different microstructures. Their structure-regulated performances in LIBs are also elucidated. We hope that this short review will provide a practical guidance for battery chemists to improve the cathode performances via elegant structural designs.

2. Microstructure design, kinetically controlled preparation of cathode materials and their regulated electrochemical performances

2.1. LiFePO$_4$

2.1.1. LiFePO$_4$ nanoparticles, nanorods and nanoplates.
Since the first discovery by Goodenough and coworkers in 1997, olivine LiFePO$_4$ (LFP) has attracted great research
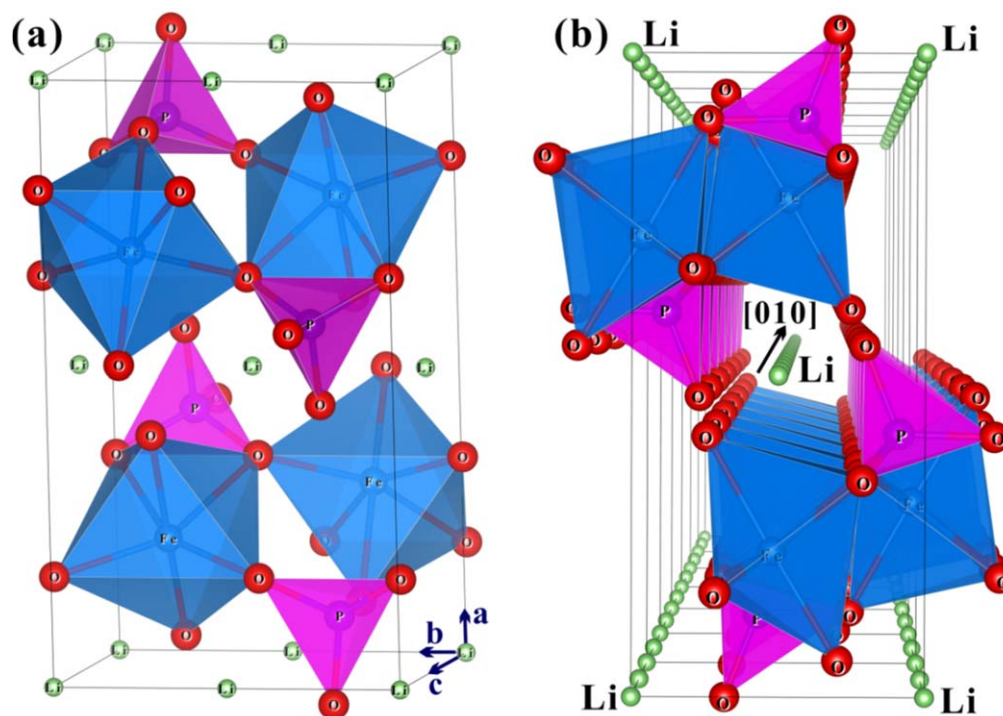
Figure 2. (a) The crystal structure of LiFePO$_4$ and (b) the perspective view of the structure along [010] direction.

interests [14]. As a polyanion cathode material, LiFePO$_4$ displays good electrochemical performances, together with many advantages, such as low cost, high stability and environmental benignity. As shown in figure 2(a), the structure can be viewed as slightly distorted *hcp* oxygen arrays with 1/2 of the octahedral sites seated by Fe^{2+} and 1/8 occupied by Li$^+$. Both the edge-shared LiO$_4$ and corner-shared FeO$_6$ octahedra run parallel to the *c* axis and propagate along *b* axis. As presented in figure 2(b), lithium ions are constraint by the surrounding PO$_4$ tetrahedra and form one-dimensional conduction channel along the [010] direction [1, 14]. This anisotropic feature implies that the microstructures of LFP cathodes can greatly influence their electrochemical performances.

In view of this, we have designed a simple sodium dodecyl benzene sulfonate (SDBS) mediated hydrothermal method to prepare morphology-controlled LiFePO$_4$ materials [15]. SDBS, functioning as a chelation agent, has strong binding capability to specific crystallographic surfaces, to direct the growth of LFP nanostructures. According to Wulff construction theory, the equilibrium shape of olivine LFP is polyhedral particulate with (010) facet contributing large portion of the total surface area, since it has lower surface energy than others [16]. Without SDBS in the synthetic recipes, only LFP nanoparticles (figures 3(a)–(c)) can thus be obtained under the thermodynamically equilibrium hydro-thermal condition, which is close to the Wulff shape of olivine LFP. A small amount of SDBS (e.g. 0.0006 M) may be preferentially adsorbed on the (010) facet to further reduce its surface energy. Therefore, rod-like LFP, with increased ratio of exposed (010) facet was achieved (figures 3(d)–(f) and 4(a)–(b)). An even more coverage by SDBS molecules

(e.g. 0.003 M) further enhance the dominance of (010) facet in the finally exposed surfaces, by forming the plate-like LFP microstructures (figures 3(g)–(i) and 4(c)–(d)), which can be viewed as the LFP nanorods thinned along [010] direction. Other surfactants, such as ethylene glycol and diethylene glycol, could have similar effect in the guided growth of facet-controlled LFP nanosheets [16].

However, the low electronic conductivity, on the order of 10^{-9} S cm^{-1} at room temperature, has become the main obstacle for the application olivine LiFePO$_4$ cathode materials [15, 17]. From the structural point of view, the corner-sharing FeO$_6$ octahedra of LiFePO$_4$ are spatially separated by PO$_4$ tetrahedra, which interrupt the electron conduction via continuous FeO$_6$ frameworks. A simple but scalable approach is the surface modification of LFP by conductive carbon layers.

The carbon-coated LFP nanoplates reported above show the longest charge–discharge plateau in comparison with the nanoparticle and nanorod counterparts (figures 5(a)–(c)). As compared in figure 5(d), the LFP nanoplates also display the best rate performances among three different LFP samples. The different microstructures are believed to be responsible for their different electrochemical performances. The thickness of the nanoplate LFP is only 20 nm along *b* axis, whereas the other two have much large thickness. The conduction of Li$^+$ is thus more facilitated along such direction. The special microstruc-ture endows LFP nanoplates much lower charge transfer resistance (R_{ct}) of 48.7 Ω than LFP nanorods (R_{ct} = 93.1 Ω) and nanoparticles (R_{ct} = 142.5 Ω) (figure 5(e)). The Warburg impedance coefficient of LFP nanoplates is also much lower than these of LFP with nanorod and nanoparticle morphologies (figure 5(f)).
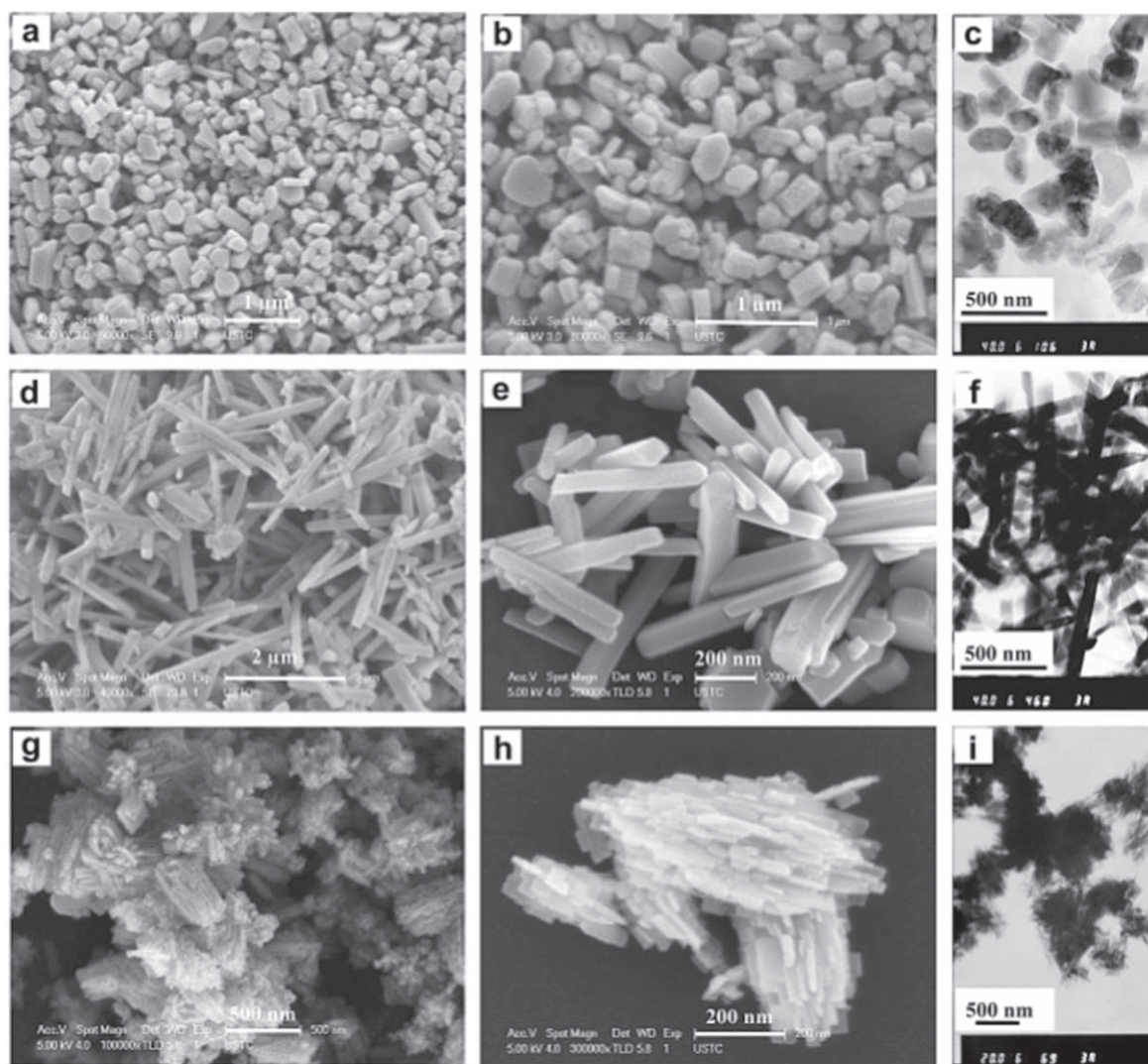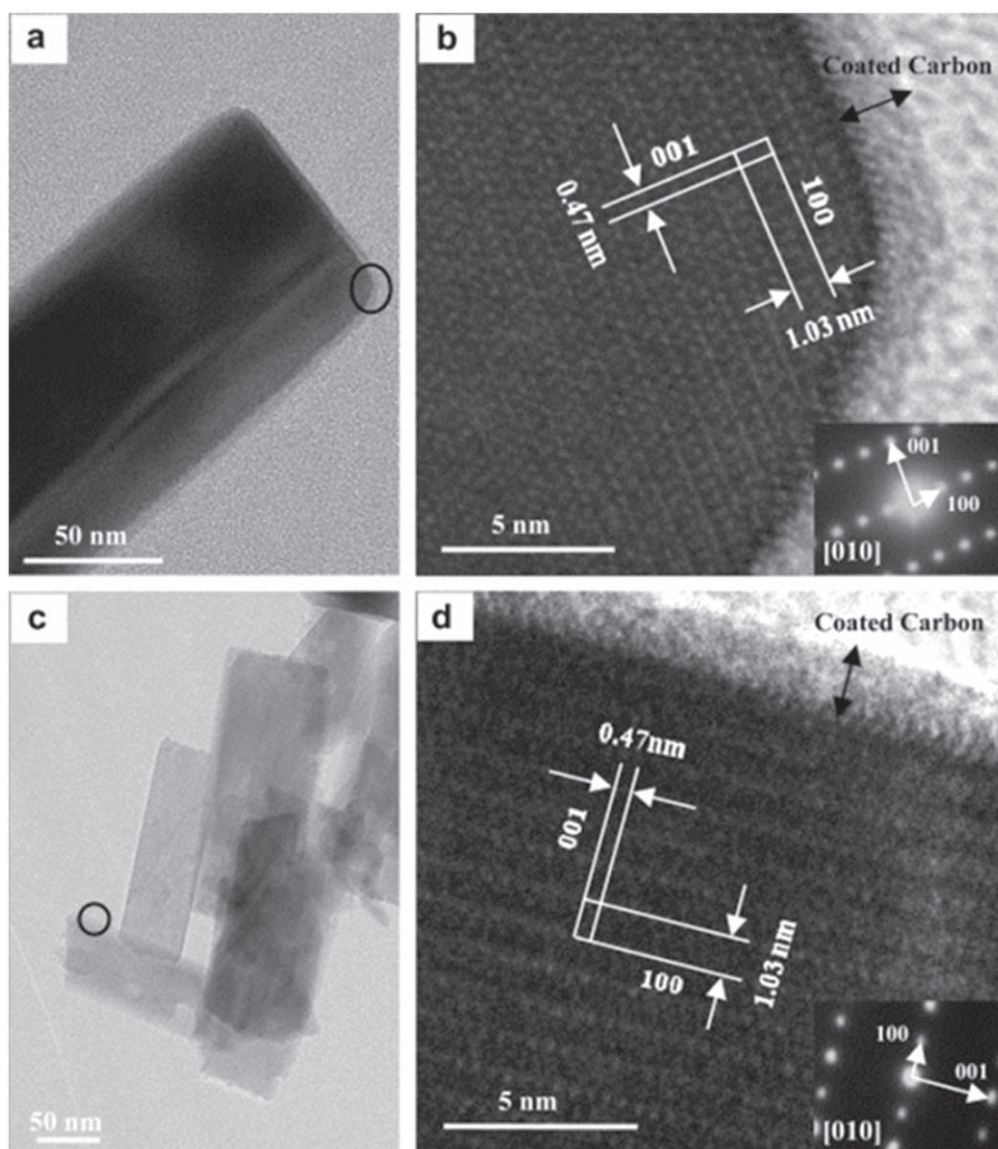
Figure 3. FESEM and TEM images of different LFP/C microstructures: (a)–(c) nanoparticles, (d)–(f) nanorods, (g)–(i) nanoplates. Reprinted from [15], Copyright 2012, with permission from Elsevier.

2.1.2. Hierarchical LiFePO$_4$ microflowers. The nanoplate building blocks of LFP can be assembled to reduce their surface energies. We have also synthesized hierarchical LiFePO$_4$ microflowers via a solvothermal template method [18]. The pre-formed NH$_4$FeP$_2$O$_7 \cdot 1.5$H$_2$O rectangular nanoplates were heated in ethanol with appropriate amounts of LiCl and N$_2$H$_4 \cdot$ H$_2$O in an autoclave. During the solvothermal reaction, the NH$_4$FeP$_2$O$_7 \cdot 1.5$H$_2$O nanoplates were reduced by N$_2$H$_4 \cdot$ H$_2$O and intercalated by Li$^+$ cations. The flower-like hierarchical microstructures of LiFePO$_4$ were eventually obtained (figure 6). Each assembly was stacked by many nanoplate building blocks. It should be noted that the solvent used during the solvothermal treatment play a significant role in the assembly of the hierarchical structures. For instance, when H$_2$O/ethanol (volume ratio $= 1/7$) mixed solvent was used, only octahedral-shaped LiFePO$_4$ could be obtained.

As shown in figures 7(a) and (b), the carbon coating layer on LiFePO$_4$ nanoplate is smooth, with the thickness of about 5 nm. The carbon-coated hierarchical LiFePO$_4$ microstructures

delivered discharge capacities of 146, 135, 121 and 101 mAh g^{-1} at the current densities of 0.5, 1, 2, 5 and 10 C, respectively (figure 7(c)). The rate capability of LiFePO$_4$ hierarchical microstructures is significantly higher than that of the octahedral-shaped counterpart at the respective current densities. The hierarchical LiFePO$_4$ microflowers also display good cycling performance, with a low capacity decay after 70 cycles at 1 C rate (figure 7(d)). The enhanced electrochemical performances are ascribed to the hierarchical microstructures that have higher structural integrity which improves the electrochemical stability [18].

2.1.3. LiFePO$_4$ microplates with exposed (010) face. As discussed above, 1D Li$^+$ conduction channel in olivine-type LiFePO$_4$ is along the [010] crystallographic direction. Therefore, plate-like LiFePO$_4$ microstructure with larger exposed area of (010) facet is expected to have shorter diffusion path for Li$^+$ ions, for which the enhanced electrochemical performances are possible. In view of this, we have proposed a solvothermal approach to synthesize

Figure 4. HRTEM images of different LFP/C microstructures: (a), (b) nanorods, (c), (d) nanoplates. Insets are corresponding SAED patterns. Reprinted from [15], Copyright 2012, with permission from Elsevier.

hierarchical LiFePO$_4$ microplates exposing large proportion of (010) facets [19]. Different from the above method which used NH$_4$FeP$_2$O$_7 \cdot$ 1.5H$_2$O rectangular nanoplate template, this approach does not rely on any template. The hierarchical LiFePO$_4$ microplates can be readily obtained by reducing the amorphous FePO$_4$ particles by N$_2$H$_4 \cdot$H$_2$O. The reaction occurs in an autoclave under 180 $^\circ$C with pure ethanol as the reaction solvent.

As shown in figures 8(a)–(b), the LiFePO$_4$ microplates have regular plate-like morphology with the average diameter of about 2.5 μm and thickness of 200–500 nm. The hierarchical LiFePO$_4$ microplates consist of many sheet-like building blocks with the thickness of about 10 nm (figures 8(c)–(d)). The TEM images show the uniform carbon coating with the thickness of about 4 nm on the surface of LiFePO$_4$ microplates (figures 8(e)–(f)). More importantly, the exposed surface of the microplate is dominated by (010) facet that is expected to facilitate the diffusion of Li$^+$.

The electrochemical performances of the two LFP cathodes show significant differences. As shown in figures 9(a)–(c), the LFP microplates display superior capacity and rate performance to the flower-like counterparts. For example, the discharge capacity for LFP microplates are 157 and 105 mAh g^{-1} at 0.1 C and 10 C respectively, significantly higher than the corresponding values for LFP microflowers (144 and 65 mAh g^{-1} at 0.1 C and 10 C, respectively). The enhanced electrochemical performances of LFP microplates are believed to be resulted from their structural feature that improves the electrochemical reversibility and facilitates the diffusion of Li ions by reducing the charge transfer resistance (figure 9(d)).

2.2. LiMn$_2$O$_4$ spinel

2.2.1. LiMn$_2$O$_4$ microspheres. The ideal spinel LiMn$_2$O$_4$ exists in the space group of $Fd\bar{3}m$, with the anions forming a
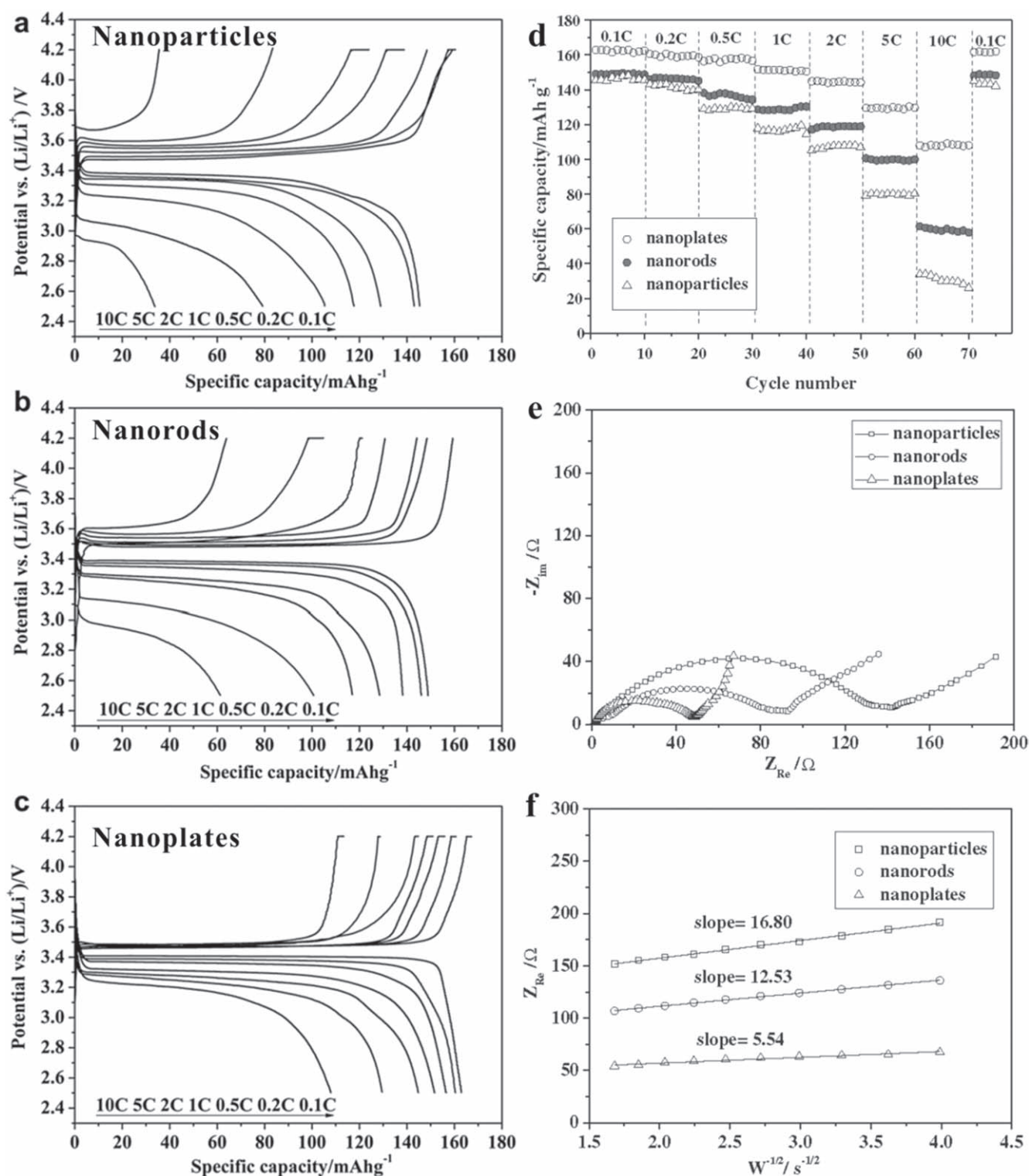
Figure 5. (a)–(c) The initial charge–discharge curves, (d) rate performance, (e) electrochemical impedance spectroscopy, (f) the relationship between Z_{Re} and $\Omega^{-1/2}$ for LiFePO$_4$ of different microstructures: (a) nanoparticles, (b) nanorods and (c) nanoplates. Reprinted from [15], Copyright 2012, with permission from Elsevier.

face-centered cubic packing and occupying 32e sites (figure 10(a)). Li ions are located at the tetragonal 8a sites, while Mn cations take the octahedral 16d sites and the octahedral 16c sites remain empty [21]. If molar fraction of Li$^+$ exceeds 1 (Li$_{1+x}$Mn$_{1-y}$O$_4$), the lithium ions enter the vacant 16c sites (figure 10(b)) [20]. The 8a and empty 16c

sites in spinel LiMn$_2$O$_4$ form a three-dimensional pathway for Li$^+$ diffusion [20]. With a theoretical capacity of 148 mAh g^{-1}, LiMn$_2$O$_4$ has become a popular cathode material, due to its privilege of low cost, high voltage (4.0 V versus Li/Li$^+$) and good environmental amity [6]. However, LiMn$_2$O$_4$ cathode materials suffer from serious
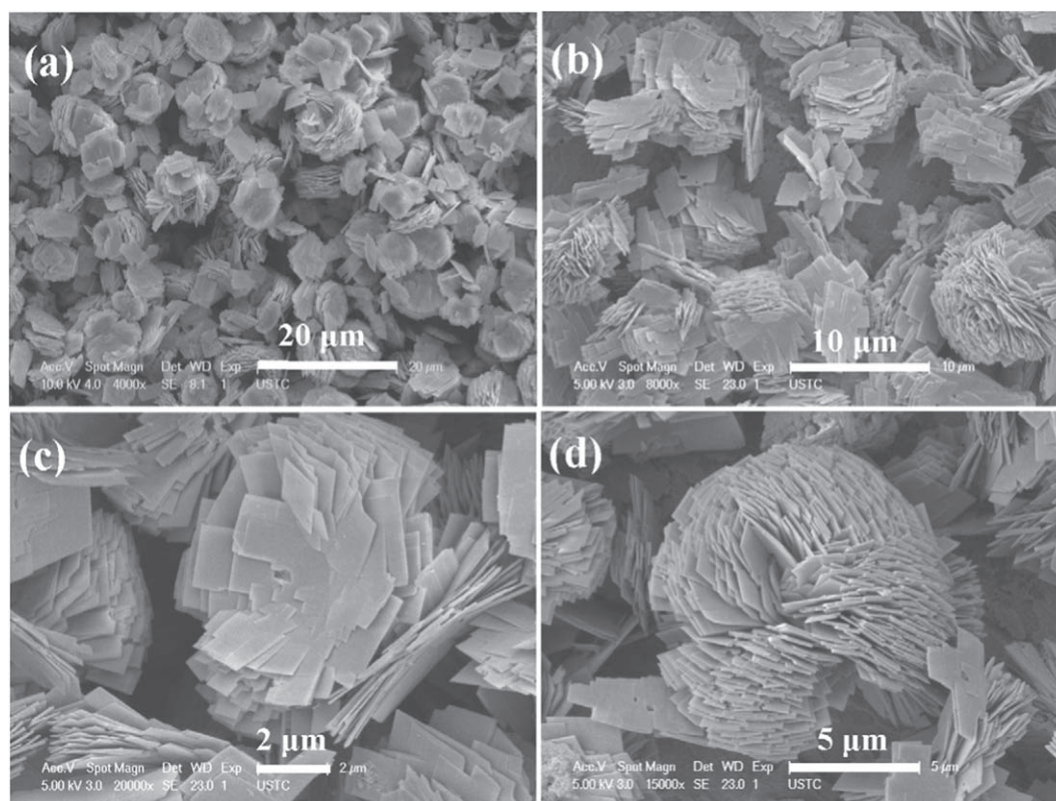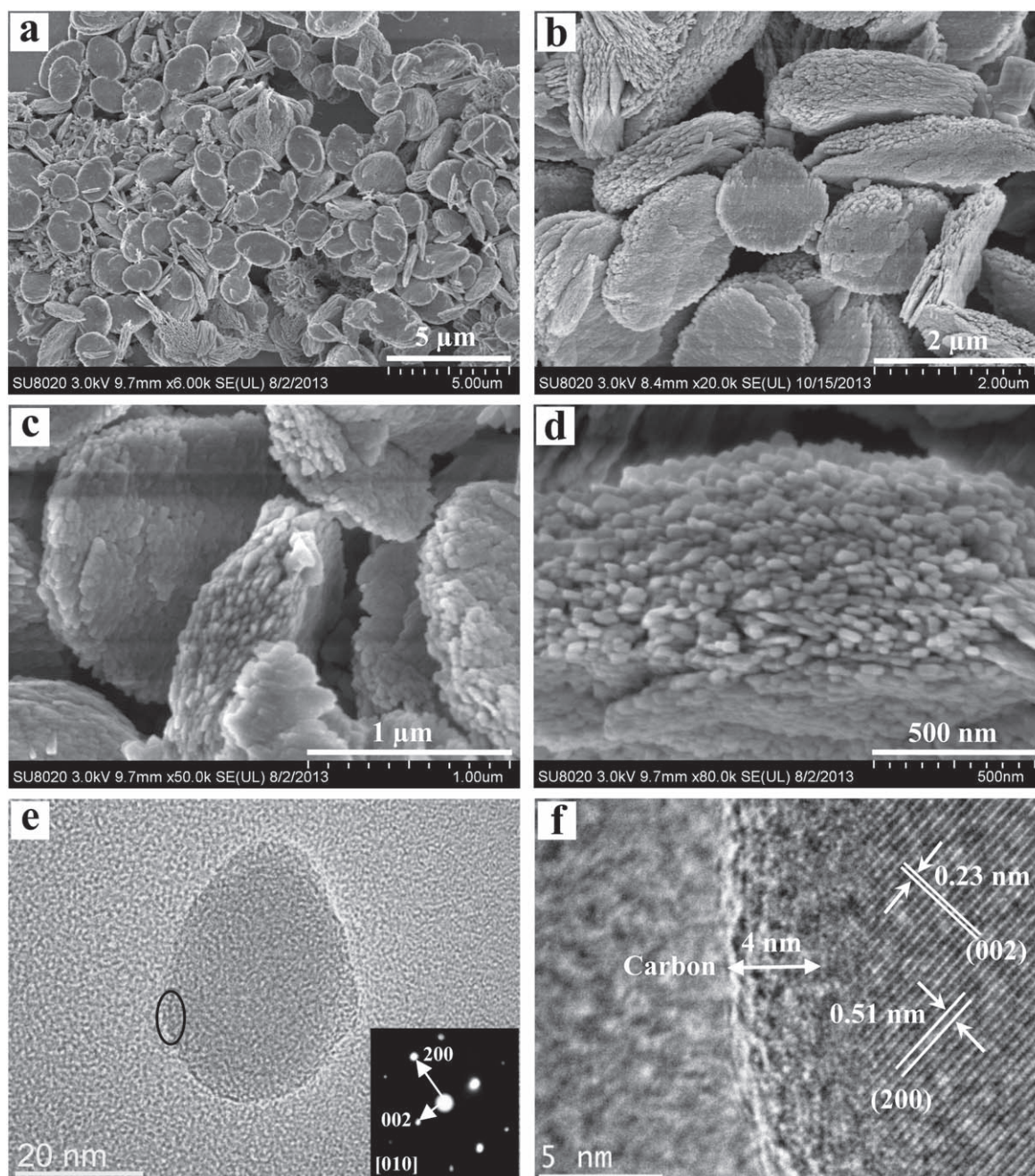
Figure 6. FESEM images of the carbon-coated LiFePO$_4$ hierarchical microflowers in different magnifications. Reprinted from [18], Copyright 2011, with permission from Elsevier.
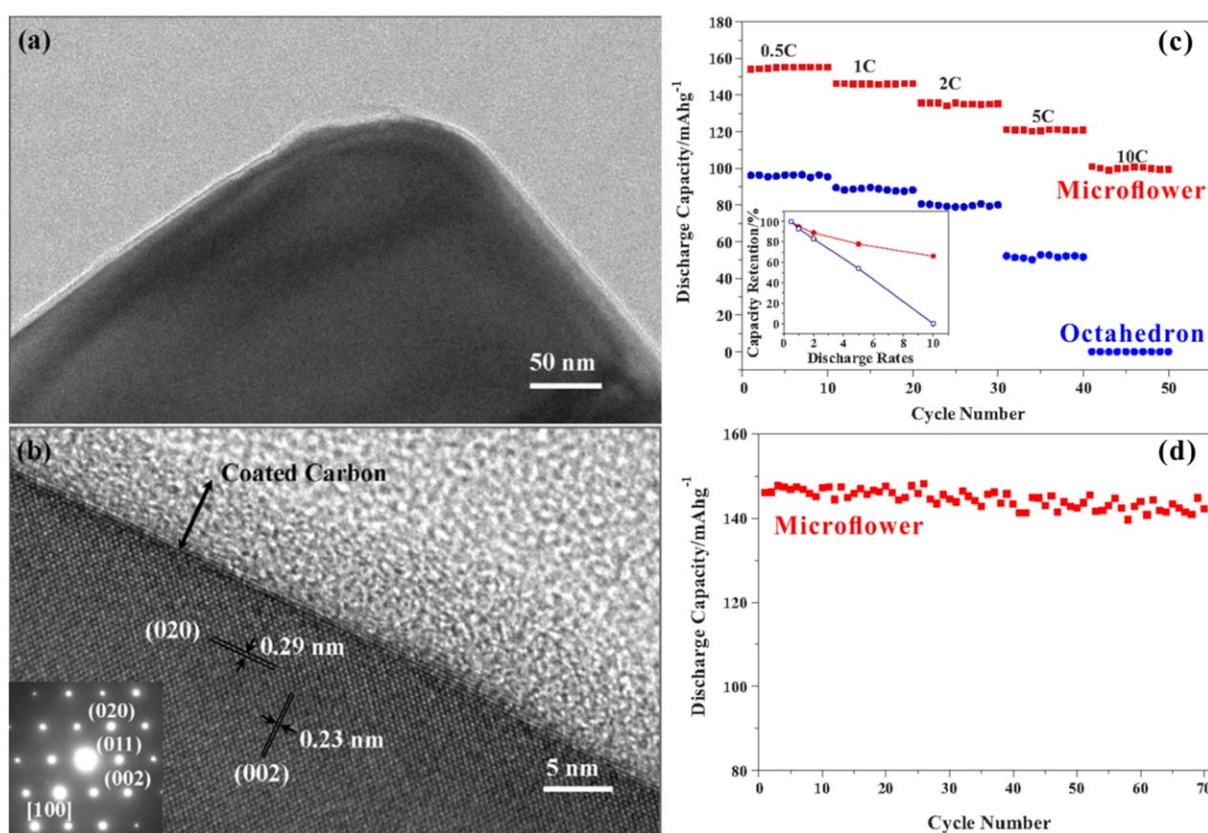
Figure 7. (a) TEM and (b) HRTEM images of a single LiFePO$_4$ nanoplate on LFP microflowers; (c) the rate capabilities of LiFePO$_4$ hierarchical microflowers and octahedrons; (d) the cycling performance of LiFePO$_4$ microflowers at 1 C. Reprinted from [18], Copyright 2011, with permission from Elsevier.

Figure 8. (a)–(d) FESEM images of carbon-coated LiFePO$_4$ microplates; TEM images of (e) the whole and (f) a part of a single plate. Reprinted with permission from [19]. Copyright 2014 American Chemical Society.

capacity fading. An important reason is the dissolution of Mn cations into the electrolyte caused by H$^+$ corrosion. An effective approach is increasing the particle size of LiMn$_2$O$_4$ active material to reduce the surface area accessible to the electrolyte, which cannot only reduces Mn dissolution, but also increase the electrode density [20]. Conversely, the large particles can deteriorate the rate performance. Therefore, synthesizing LiMn$_2$O$_4$ bulky particle consisting of aggregated nano-sized particles is a simple but effective approach to improve the electrochemical performances of LiMn$_2$O$_4$ cathode materials [20].

We have completed the successful preparation of LiMn$_2$O$_4$ microspheres via a facile co-precipitation method

[22]. 1.379 g of LiNO$_3$ was dissolved in 2 ml of deionized water before it was mixed with 4.65 ml of Mn(NO$_3$)$_2$ solution (50 wt%). 6 g of (NH$_4$)$_2$CO$_3$ was dissolved in 8 ml of deionized water in a separate container. The pink mixed solution of LiNO$_3$ and Mn(NO$_3$)$_2$ was added dropwisely into the (NH$_4$)$_2$CO$_3$ solution to obtain white precipitates. The metal carbonate precursor decomposed into LiMn$_2$O$_4$ product upon subsequent drying and thermal annealing processes. The XRD patterns (figure 11(a)) confirm the formation of cubic phase of spinel LiMn$_2$O$_4$ (JCPDS card no. 35-0782). By analyzing the full width at half maximum of the diffraction peaks, we learn that larger LiMn$_2$O$_4$ particles with better crystallinity can be obtained by increasing the annealing
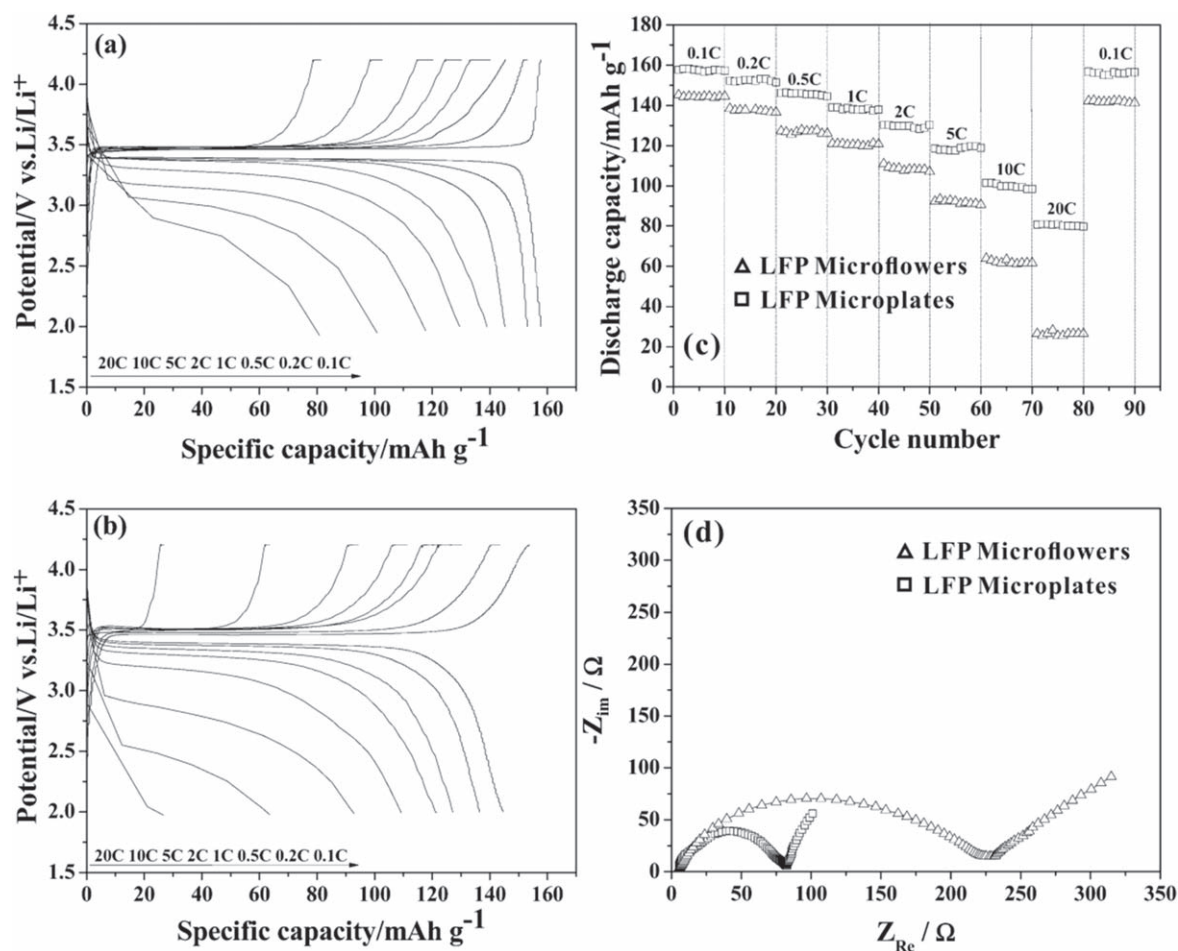
Figure 9. The charge–discharge profiles for (a) LFP microplates and (b) LFP microflowers; (c) the rate performance and (d) electrochemical impedance spectra for the two different LFP samples. Reprinted with permission from [19]. Copyright 2014 American Chemical Society.
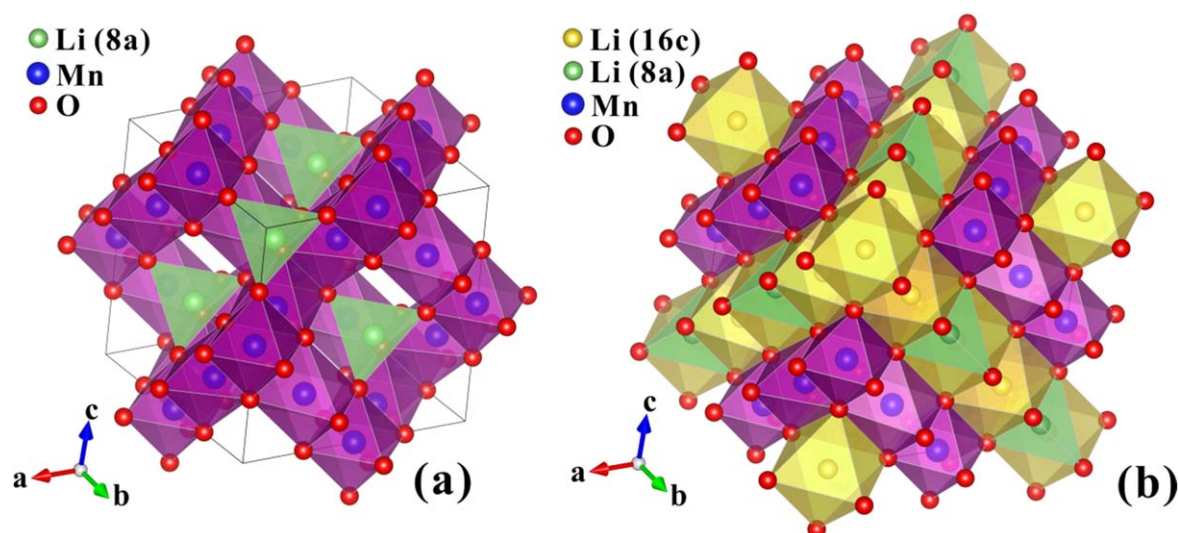
Figure 10. Crystal structure of (a) $LiMn_2O_4$ and (b) $Li_{1+x}Mn_{2-x}O_4$. Green balls: Li at tetragonal 8a sites. Yellow balls: Li at octahedral 16c sites. Blue balls: Mn at octahedral 16d sites. Red balls: O at 32e sites.

temperatures or times. A typical $LiMn_2O_4$ sample prepared by annealing at 750 °C for 9 h displays spherical morphology with the size of about 600–900 nm, assembled by 30–40 nm nanoparticles.

This featured microstructure of $LiMn_2O_4$ gives rise to its good electrochemical performances. As shown in figure 12(a), the typical charge–discharge curves of $LiMn_2O_4$ microspheres prepared at 750 °C for 9 h display two voltage plateaus which
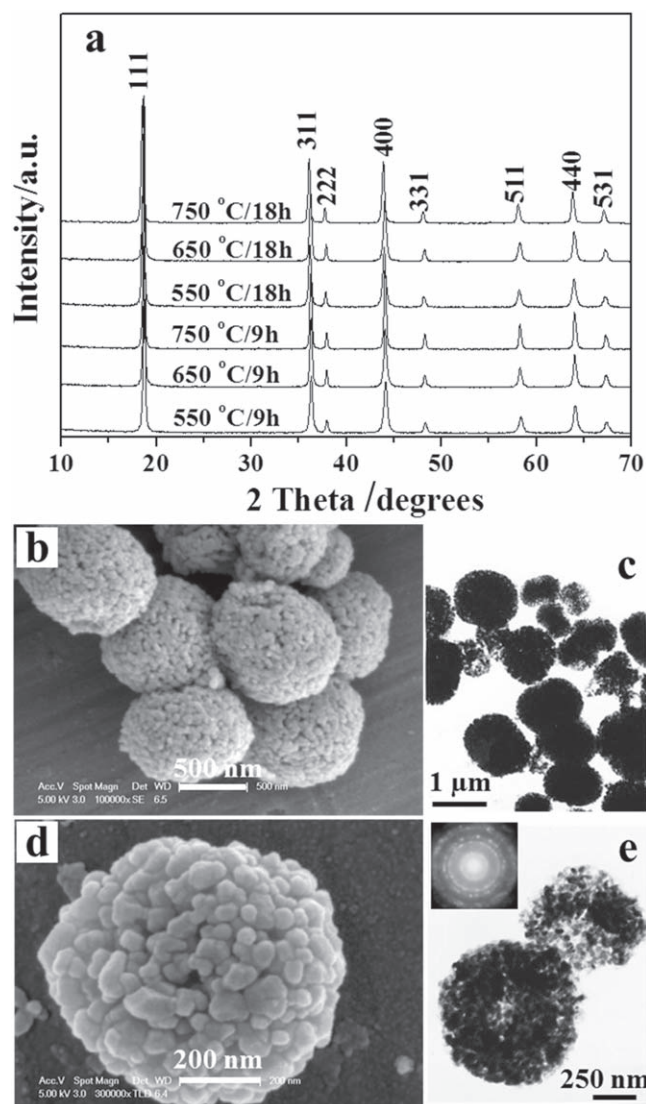
Figure 11. (a) XRD patterns of $LiMn_2O_4$ samples prepared with different annealing times and temperatures; (b), (d) SEM images and (c), (e) TEM images of $LiMn_2O_4$ sample annealed at 750 °C for 9 h.

are within the ranges of 3.9–4.0 V and 4.1–4.2 V, respectively. The two plateaus have nearly equal contributions to the overall charge/discharge capacity, which suggests that the lithiation/delithiation occur both in a two-step manner. For the charging process, $LiMn_2O_4$ is transformed into $Li_{0.5}Mn_2O_4$ at the lower-voltage plateau, followed by the further evolution into λ-MnO_2 at higher-voltage plateau [23]. For the discharging process, half of the empty tetragonal 8a sites are firstly filled by Li ions, producing single phase of $Li_{0.5}Mn_2O_4$ from λ-MnO_2. The following discharging will increase the repulsion between lithium ions at 8a sites, resulting in a small increase in the free-energy of the system. Therefore, the discharge voltage plateau is slightly reduced by about 100 mV [23]. Increasing the discharging rate from 0.1 to 1 C only leads to small polarization of the cathodes, implying the good rate capability of the $LiMn_2O_4$ microspheres (figure 12(a)). Further electrochemical analysis shows the overall trend that higher annealing

temperature and longer annealing time are beneficial to improve the cycling performances of $LiMn_2O_4$ microspheres (figure 12(b)). This should be due to the better structural stability of $LiMn_2O_4$ microspheres prepared at these conditions, as reflected by the better crystallinity obtained from XRD results.

2.2.2. $LiNi_{0.5}Mn_{1.5}O_4$ hollow spheres. As mentioned above, the capacity decay is a serious problem of spinel $LiMn_2O_4$ cathode materials, with Mn cation dissolution as one major cause. Another important cause is its structural instability related to Mn^{3+}. The Jahn–Teller (JT) distortion of Mn^{3+} in spinel $LiMn_2O_4$ causes the irreversible structural evolution from spinel to tetragonal phase [6, 20]. Fortunately, partial substitution of Mn by other metal cations has been proven to be an effective strategy to suppress the JT distortion. As a result, the structural stability and of course the cycling performance of $LiMn_2O_4$ are significantly improved.

Among the different doping derivatives, $LiNi_{0.5}Mn_{1.5}O_4$ is one of the most promising cathode materials. The doping by Ni^{2+} promotes the oxidation state of Mn to +4, thus eliminating the JT distorted Mn^{3+} and enhancing the structural stability during repeated charging/discharging cycles. The $Ni^{2+/4+}$ redox pair significantly enhance the voltage plateau to about 4.7 V versus Li/Li^+, thus offering $LiNi_{0.5}Mn_{1.5}O_4$ both high energy density and power density [6, 24].

$LiNi_{0.5}Mn_{1.5}O_4$ has two crystallographic structures: the stoichiometric ordered one in $P4_332$ space group and the other in non-stoichiometric disordered $Fd\bar{3}m$ space group (figure 13). In the disordered phase of $LiNi_{0.5}Mn_{1.5}O_4$, Ni and Mn cations randomly take the 16d octahedral positions, while Li^+ ions occupy tetrahedral 8a sites and diffuse via the empty 16c position along the 8a-16c-8a path (figure 13(a)) [24]. For the ordered $LiNi_{0.5}Mn_{1.5}O_4$, Li, Ni and Mn cations occupy 8c, 4b and 12d sites, respectively, whereas the empty sites are split into 4a and 12d positions. Li^+ ions thus have to be conducted through the empty 4a sites via 8c-4a-8c path or through the partially occupied 12d sites via 8c-12d-8c diffusion path (figure 13(b)). The ordered Ni and Mn ions retard the diffusion of Li^+ through the ordered $LiNi_{0.5}Mn_{1.5}O_4$, thus lowering the rate capability [6, 24].

The construction of hollow microstructures is an effective way to enhance the rate capability of spinel $LiNi_{0.5}Mn_{1.5}O_4$ cathode materials. We have reported the controllable synthesis of spinel $LiNi_{0.5}Mn_{1.5}O_4$ hollow spheres with micro- and nano-structures by tuning the co-precipitation reaction kinetics [8]. The ionization constant of HCO_3^{2-} is much smaller than that of CO_3^{2-}. $NaHCO_3$ is thus expected to result in much slower nucleation and growth rates of $MnCO_3$ and $NiCO_3$ than Na_2CO_3 does (figure 14). The slower nucleation and growth rates allow the nucleus to be assembled into large spherical particles to reduce the surface energy. As a result, spherical metal carbonate precursor can be obtained using $NaHCO_3$ as the precipitation agent. Controlling the heating rate during the subsequent thermal
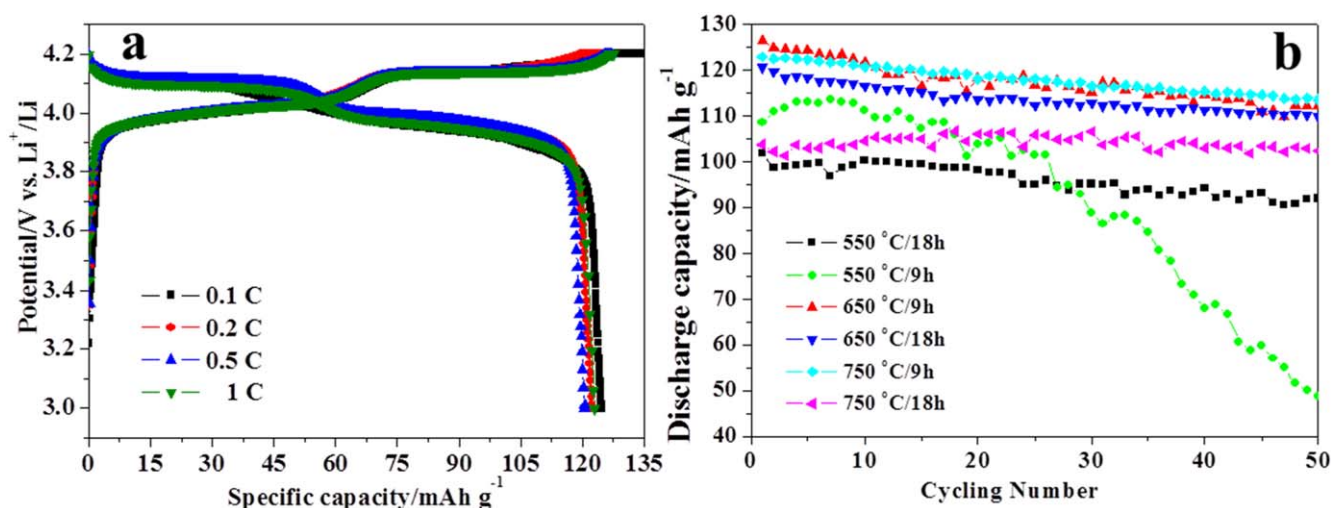
Figure 12. (a) The typical charge–discharge curves of $LiMn_2O_4$ prepared by annealing at 750 °C for 9 h; (b) the cycling performances of $LiMn_2O_4$ samples prepared at different annealing temperatures and times.
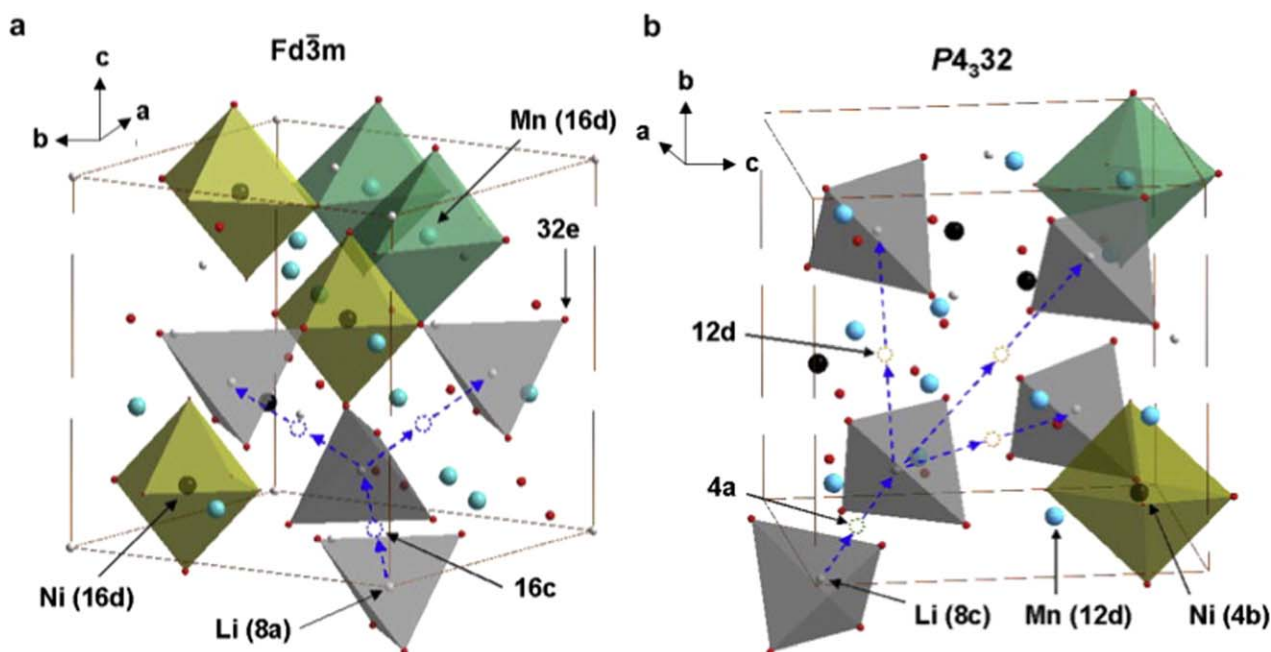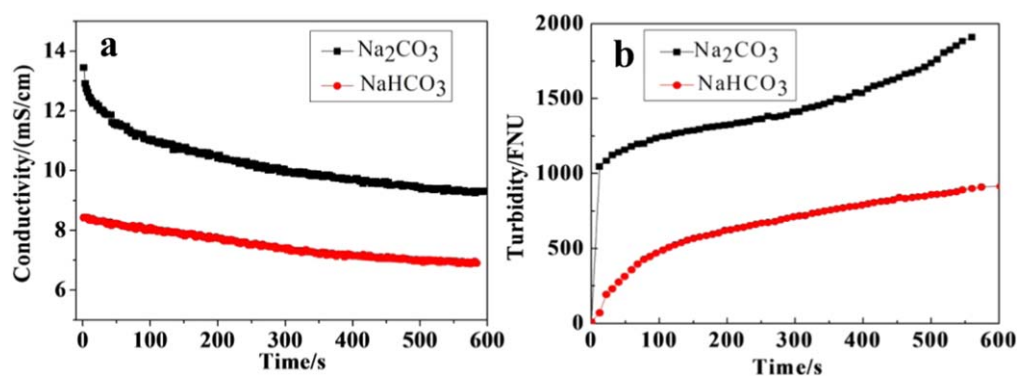

Figure 13. Lithium diffusion paths in $LiNi_{0.5}Mn_{1.5}O_4$ spinel with space group of (a) $Fd\overline{3}m$ and (b) $P4_332$. Reprinted from [24], Copyright 2012, with permission from Elsevier.
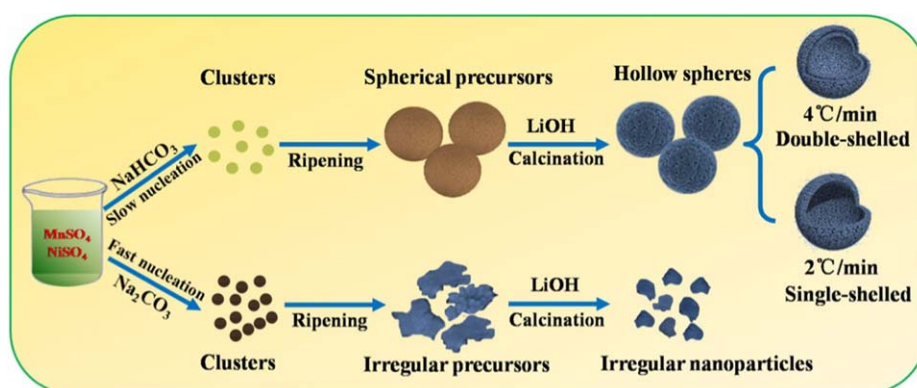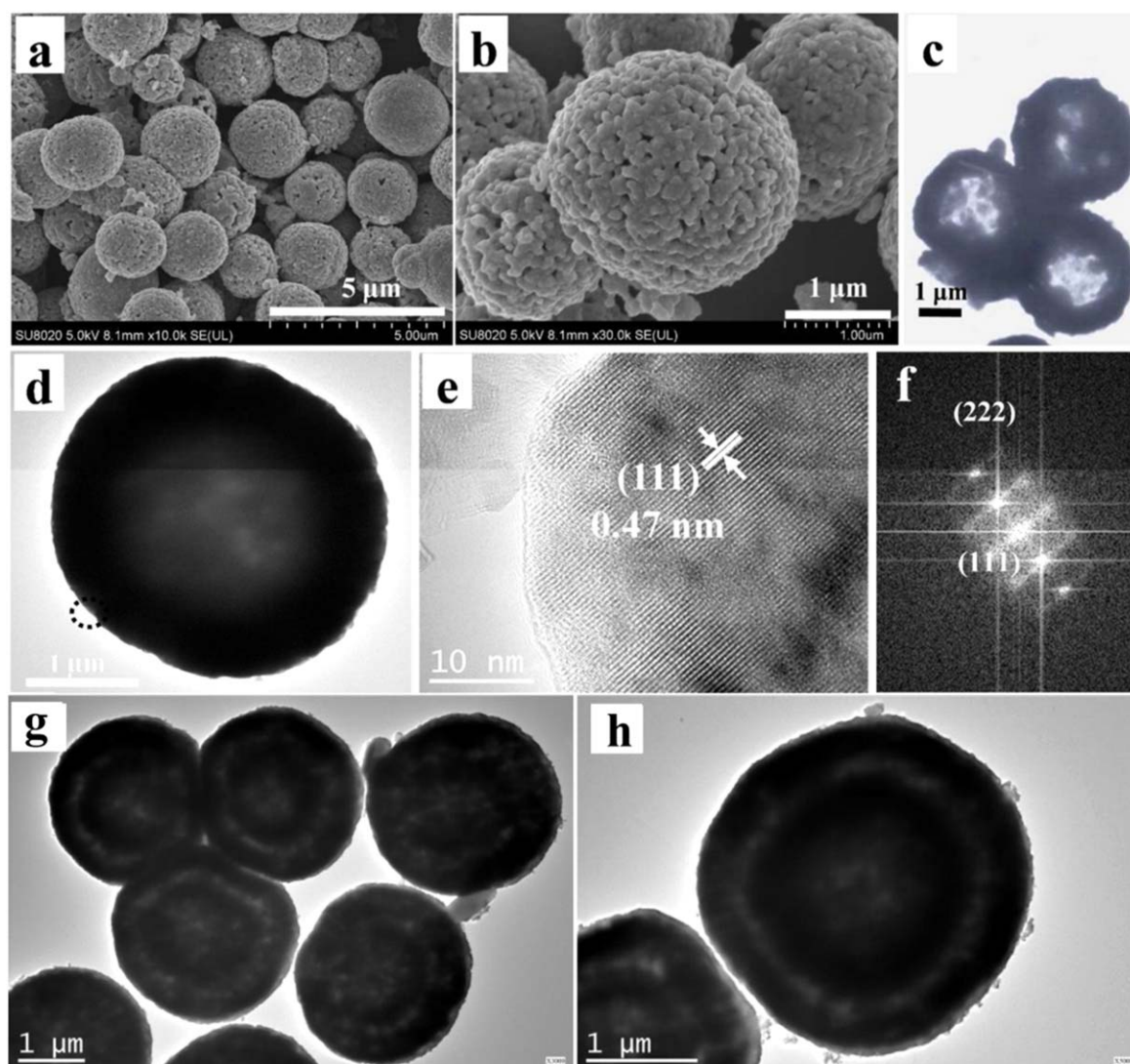

Figure 14. Schematically illustrated formation process of $LiNi_{0.5}Mn_{1.5}O_4$ hollow spheres and nanoparticles. Reprinted with permission from [8]. Copyright 2016 American Chemical Society.

Figure 15. (a) Ionic conductivity and (b) turbidity change versus time using Na_2CO_3 and $NaHCO_3$ as precipitating agent, respectively. Reprinted with permission from [8]. Copyright 2016 American Chemical Society.

Figure 16. (a), (b) FESEM, (c), (d) TEM, (e) HRTEM and (f) the FFT analysis of $LiNi_{0.5}Mn_{1.5}O_4$ hollow spheres; (g), (h) TEM images of double-shell $LiMn_2O_4$ hollow spheres. Reprinted with permission from [8]. Copyright 2016 American Chemical Society.

annealing would lead to the formation of single- or double-shell $LiMn_2O_4$ hollow spheres. With Na_2CO_3 as the precipitation agent, only carbonate precursor and the corresponding $LiNi_{0.5}Mn_{1.5}O_4$ with irregular shape could be obtained (figure 14).

The slower nucleation induced by $NaHCO_3$ has been proven by the variations of ionic conductivity and turbidity of the co-precipitation reaction system. The time-dependent ionic conductivity (figure 15(a)) suggests that the nucleation rate for $NaHCO_3$ system is much lower, which shows
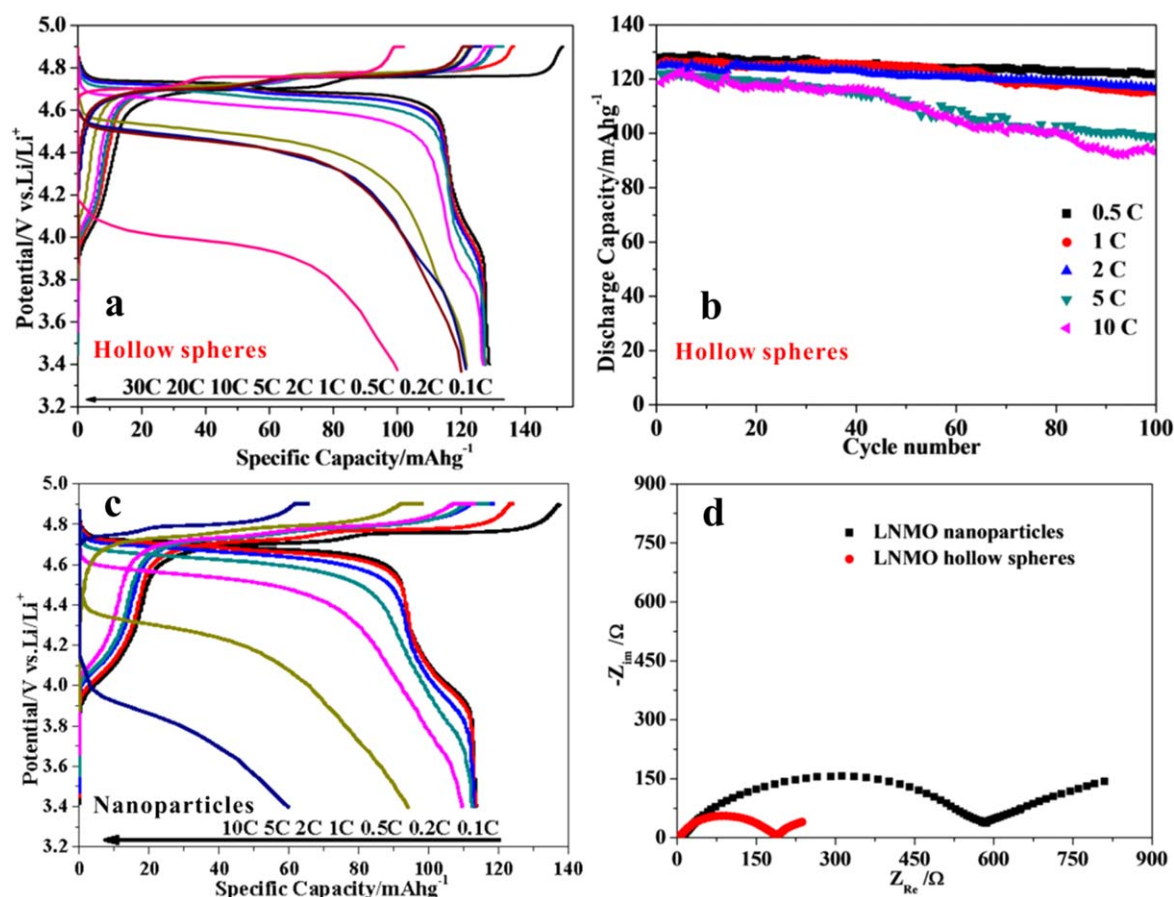
Figure 17. (a) The charge–discharge curves and (b) the cycling performances for $LiNi_{0.5}Mn_{1.5}O_4$ hollow spheres; (c) charge–discharge curves for $LiNi_{0.5}Mn_{1.5}O_4$ nanoparticles; (d) electrochemical impedance spectra. Reprinted with permission from [8]. Copyright 2016 American Chemical Society.

zero-order precipitation reaction, whereas the Na_2CO_3 system is a second-order reaction showing much faster nucleation kinetics. The turbidity curves also confirm this trend (figure 15(b)).

The SEM images (figures 16(a), (b)) show that the $LiNi_{0.5}Mn_{1.5}O_4$ product well inherits the spherical morphology of the carbonate precursor, but with hollow and porous microstructures. The $LiNi_{0.5}Mn_{1.5}O_4$ sample is composed of porous micro- and nanostructured hollow spheres with wall thickness of about 500 nm (figures 16(c), (d)). The HRTEM image and fast Fourier transform analysis further reveal the single-crystalline character of the nanoparticle building blocks for the single-shell $LiNi_{0.5}Mn_{1.5}O_4$ hollow spheres (figures 16(e), (f)). By controlling the heating rate from 2 to 4 °C min^{-1}, the double-shell $LiNi_{0.5}Mn_{1.5}O_4$ hollow spheres can be successfully obtained (figures 16(g), (h)). The different shrinking rates under controlled heating conditions are responsible for the formation of these different microstructures. When the critical stress is reached, the middle part of the carbonate precursor tends to shrink inward and leave from the pre-formed outer shell under the higher heating ramp. This leads to the splitting of different layers and formation of double-shell hollow spheres [8].

The electrochemical tests have revealed the superior performances of the hollow spheres to that of the particulate counterparts. The discharge capacity of $LiNi_{0.5}Mn_{1.5}O_4$ hollow spheres is about 130 mAh g^{-1} at the current rate of 0.1 C, which is less than 120 mAh g^{-1} for the particulate counterparts (figures 17(a), (c)). However, the double-shelled $LiNi_{0.5}Mn_{1.5}O_4$ hollow spheres do not show further enhanced electrochemical performances than the single-shelled one, probably because of the unfavorable charge transfer from the outer shell into the inner shell resulted from the void gap. At various discharging rates, $LiNi_{0.5}Mn_{1.5}O_4$ hollow spheres all display the discharge capacities much higher than those of $LiNi_{0.5}Mn_{1.5}O_4$ nanoparticles. As shown in figure 17(b), the $LiNi_{0.5}Mn_{1.5}O_4$ hollow spheres also present good cycling capabilities. Under the current rates of 0.5, 1 and 2 C, the discharge capacities only show slight decrease after 100 cycles. The capacity retention is even as high as 95% after 100 cycles at 0.5 C rate. When increasing the discharging rates to 5 and 10 C, the capacity retention can still reach 80% at 10 C after 100 cycles. The special microstructure of $LiNi_{0.5}Mn_{1.5}O_4$ hollow spheres is believed to be responsible for their superior electrochemical performances, for which the conductions of electrons and Li$^+$ ions are more facilitated, as revealed by its smaller charge transfer resistance ($R_{ct} \sim$ 190 Ω) in comparison to that of $LiNi_{0.5}Mn_{1.5}O_4$ nanoparticles ($R_{ct} \sim$ 580 Ω) (figures 17(d)).
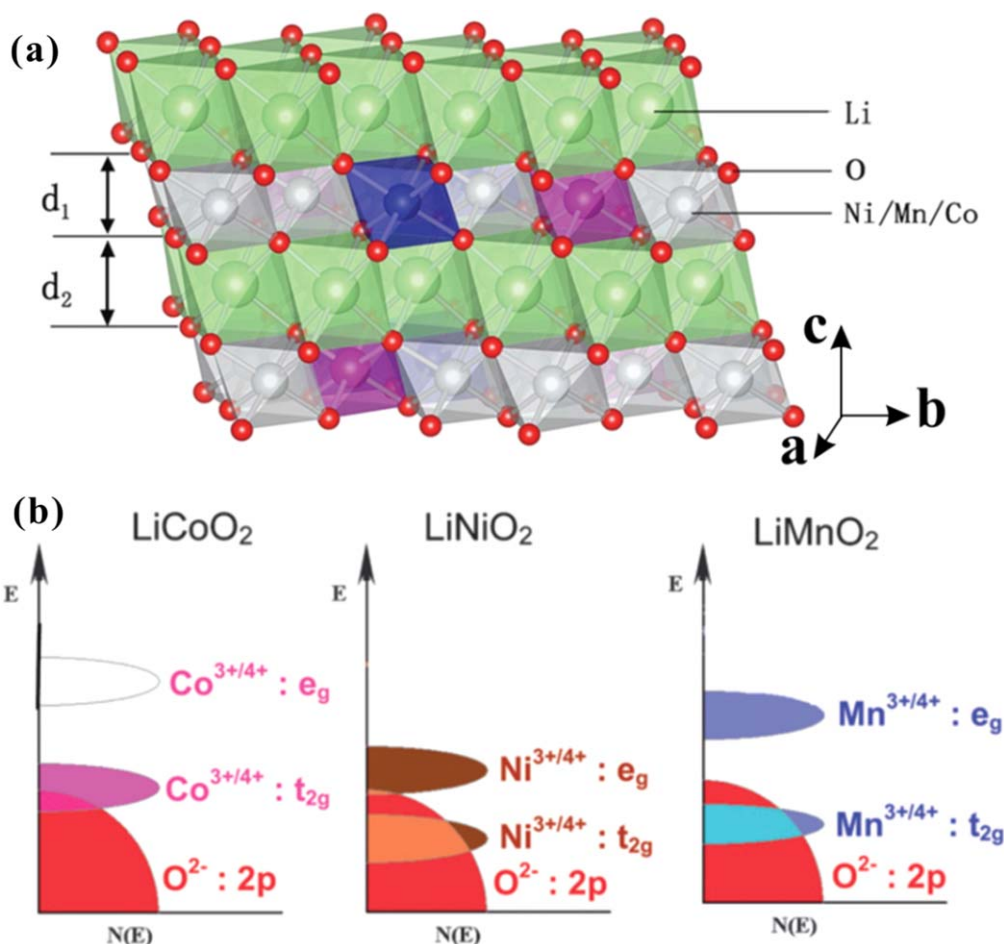
Figure 18. (a) Lattice of NCM layered structure (green atoms: Li; red atoms: O; silver/purple/blue atoms: Ni/Co/Mn transition metals). [26] John Wiley & Sons. © 2015 WILEY-VCH Verlag GmbH & Co. KGaA, Weinheim; (b) comparison of the energy diagrams of LiCoO$_2$, LiNiO$_2$ and LiMnO$_2$. Reproduced from [27] with permission from The Royal Society of Chemistry.

2.3. LiNi$_x$Co$_y$Mn$_{1-x-y}$O$_2$ layered oxides

The LiNi$_x$Co$_y$Mn$_{1-x-y}$O$_2$ (NCM) cathode materials were firstly introduced by Liu *et al* in 1999 [25]. The structure can be viewed as the solid solution of LiNiO$_2$, LiCoO$_2$ and LiMnO$_2$, due to the close ionic radii of Ni^{2+} (0.69 Å), Co^{3+} (0.54 Å) and Mn^{4+} (0.53 Å). NCM is the isostructure of LiNiO$_2$ which has the α-NaFeO$_2$ structure (Space group: $R\bar{3}m$). As shown in figure 18(a), the anions in an ideal NCM take the 6c sites to form a cubic close-packed arrangement, while Li and transition metals occupy the octahedral 3a and 3b sites, respectively, forming alternative cationic slabs along the c axis [3, 26].

Although the theoretical capacity of LiCoO$_2$ is as high as 270 mAh g^{-1}, its practical capacity is rather low, which is primarily related to its special electronic structure. The completely filled and redox active t_{2g} band of Co^{3+} in LiCoO$_2$ is well overlapping with the O^{2-} 2p band (figure 18(b)) [27]. During charging process (oxidation of Co^{3+}), the electrons in Co^{3+} t_{2g} band starts to lose, followed by the loss of O^{2-} 2p electrons when the Fermi level is pinned at the top of O^{2-} 2p band. Maximally half of an electron in t_{2g} orbital can be extracted during charging LiCoO$_2$ without inducing the oxidation of O^{2-}, otherwise the

structure will collapse due to the release of O$_2$. This corresponds to a reversible capacity of 140 mAh g^{-1} around 4 V versus Li/Li$^+$ [27].

In contrast, the redox active e_g band of Ni^{3+} barely touches the top of O^{2-} 2p band in LiNiO$_2$, even though the filled t_{2g} band completely overlaps with O^{2-} 2p. Therefore, the single electron in the redox active e_g band can be sufficiently extracted during charging, giving rise to its significantly high theoretical capacity of 270 mAh g^{-1} and a practical capacity of over 200 mAh g^{-1} [7]. Even for LiMnO$_2$, the e_g band of the high-spin Mn^{3+} lies well above the O^{2-} 2p band, implying its strong structural stability during charging-discharging process [27]. However, LiNiO$_2$ and LiMnO$_2$ suffer from their own intrinsic problems. For instance, LiNiO$_2$ always has non-stoichiometric compositions due to lithium loss and reduction of Ni^{3+} to Ni^{2+} during thermal calcination and cation mixing due to the very close ionic radii of Ni^{2+} (0.69 Å) and Li$^+$ (0.71 Å) [2, 3]. The octahedral coordinated Mn^{3+} in LiMnO$_2$ is JT distorted, which leads to the transition of layered LiMnO$_2$ to spinel structure during repeated electrochemical cycling [27].

However, in LiNi$_x$Co$_y$Mn$_{1-x-y}$O$_2$ materials, the single e_g electron in high-spin Mn^{3+} has the strong tendency to be transferred to Ni^{3+}, resulting more energetically favorable
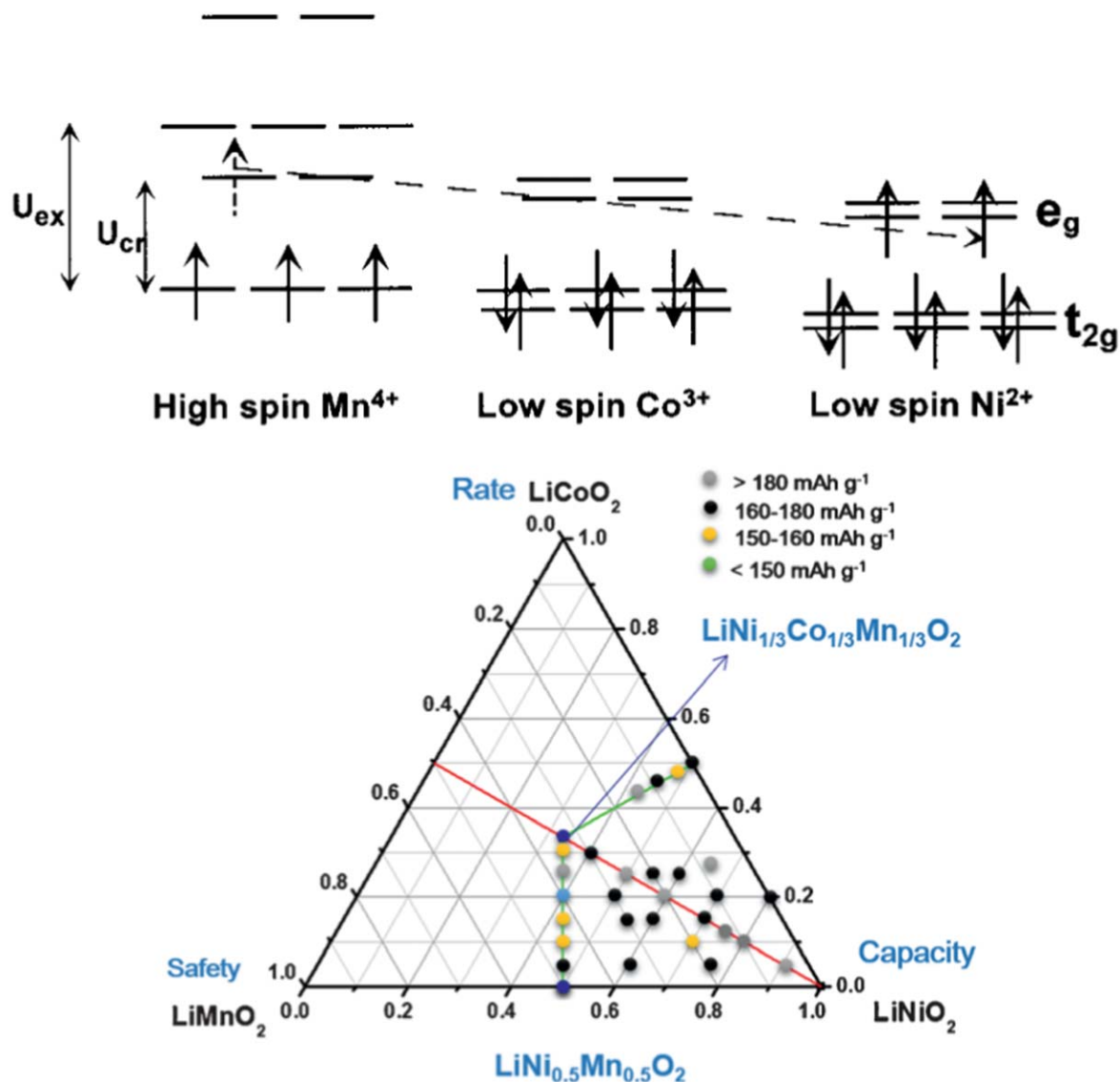
Figure 19. (a) Schematic of d-electron levels in LiNi$_x$Co$_{1-2x}$Mn$_x$O$_2$ (U_{Cr} is the crystal field splitting energy and U_{ex} is the exchange energy.). (Reproduced with permission from J. Electrochem. Soc., 2002, 149, A3066. Copyright 2012, The Electrochemical Society); (b) compositional phase diagrams of lithium stoichiometric-layered transition-metal oxide: LiCoO$_2$-LiNiO$_2$-LiMnO$_2$. The positions indicated by dots represent the described LiNi$_x$Co$_y$Mn$_{1-x-y}$O$_2$ materials. [7] John Wiley & Sons. © 2015 WILEY-VCH Verlag GmbH & Co. KGaA, Weinheim.
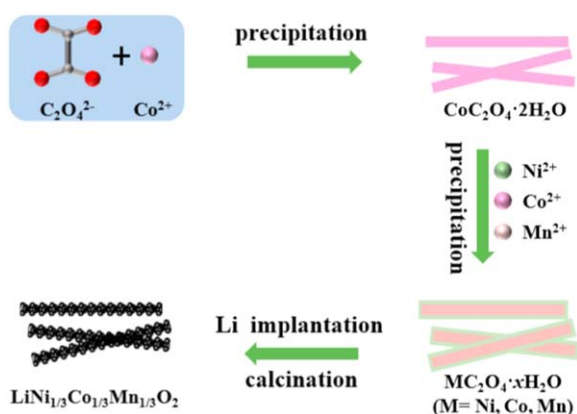
Figure 20. Schematic diagram of stepwise co-precipitation approach for NCM111 microrods. Reprinted from [29], Copyright 2014, with permission from Elsevier.

Ni^{2+} and JT inactive Mn^{4+} (figure 19(a)) [28]. Increasing the Mn proportion in NCM will significantly improve the structural stability and of course the cathode safety. The Ni^{2+}/Ni^{4+} redox couple in NCM can further enhance the capacity in comparison with Ni^{3+}/Ni^{4+} active couple. Increasing Ni content is thus beneficial for the improvement of the cathode capacity. The smaller radius of Co^{3+} could inhibit the migration of Ni^{2+} into Li$^+$ layer, thus stabilizing the structure and improving the Li$^+$ diffusion kinetics. In addition, the electrical conduction is more facilitated in LiCoO$_2$. Therefore, increased Co content can thus yield better rate performance of NCM cathode materials (figure 19(b)) [2, 7]. To date, various compositions of NCM have been explored, with LiNi$_{1/3}$Co$_{1/3}$Mn$_{1/3}$O$_2$ (NCM111 and alternatively called as 333), LiNi$_{0.4}$Co$_{0.2}$Mn$_{0.4}$O$_2$ (NCM424), LiNi$_{0.5}$Co$_{0.2}$Mn$_{0.3}$O$_2$ (NCM523), LiNi$_{0.6}$Co$_{0.2}$Mn$_{0.2}$O$_2$
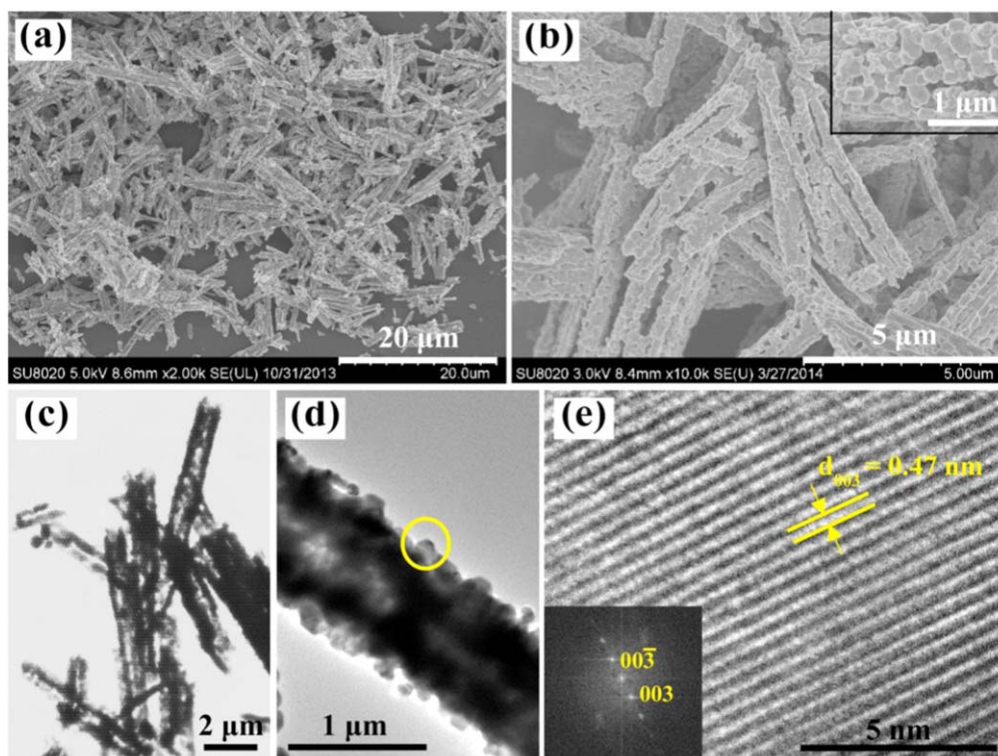
Figure 21. (a), (b) FESEM images, (c), (d) TEM images, (e) HRTEM image of NCM111 microrods. The inset of (e) is the corresponding FFT image. Reprinted from [29], Copyright 2014, with permission from Elsevier.

(NCM622) and $LiNi_{0.8}Co_{0.1}Mn_{0.1}O_2$ (NCM811) as well known representatives.

2.3.1. $LiNi_{1/3}Co_{1/3}Mn_{1/3}O_2$ microrods.

The microstructures of the cathode materials have strong influences on the diffusion of electrons and ions during charging and discharging processes. We have reported a simple strategy to prepare $LiNi_{1/3}Co_{1/3}Mn_{1/3}O_2$ 1D hierarchical microrods via a stepwise co-precipitation method [29]. As shown in figure 20, the synthesis has taken full advantage of the crystallization habit of $CoC_2O_4 \cdot 2H_2O$ to form rod-like cobalt oxalate precursor in the first precipitation step. The $CoC_2O_4 \cdot 2H_2O$ microrods served as the seed to template the growth of other metal oxalates during the subsequent co-precipitation step. After lithium implantation at high temperature, porous and rod-like NCM111 materials can be achieved.

The FESEM images indicate that the sample is mainly composed of NCM111 microrods with diameters of about 1 μm and lengths of about 10 μm (figures 21(a)–(d)). The NCM111 microrods are assembled by many sub-micron particles with the sizes of 200–400 nm and possess plenty of porous and void space in the rod. The primary particle building blocks are merged with adjacent ones in the rod-like morphology (figures 21(c), (d)). The HRTEM and FFT pattern confirm the (003) plane of the $LiNi_{1/3}Co_{1/3}Mn_{1/3}O_2$ phase [29].

Due to the unique porous and 1D structures, the NCM111 microrods have exhibited good electrochemical performances as the cathode materials in LIB. As presented in figure 22(a), the first discharge capacity of NCM111 microrods is 163.3 mAh g^{-1} with the corresponding coulombic efficiency of 92% at 0.1 C. The discharge capacities are 135.3 mAh g^{-1} and 126.9 mAh g^{-1} at 5 C and 10 C, respectively, both better than those of the microparticle counterparts [29]. The rate capability and cycling performance for NCM111 microrods (denoted as NCM-MRs) are also superior to those of the NCM111 microparticles (denoted as NCM-MPs) (figures 22(b)–(c)). The superior electrochemical performances have also been revealed by the electrochemical impedance spectroscopy. Obviously, NCM111 microrods show a charge transfer resistance of 69.6 Ω, significantly lower than that of NCM111 microparticles (151.2 Ω) (figure 22(d)). The superior electrochemical performances of NCM111 microrods should be attributed to the 1D rod-like structure that can readily relieve the strain during repeated electrochemical cycling and thus maintain the structural integrity. In addition, the 1D hierarchical microrod structure can provide appropriate contact area between electrode and electrolyte and effectively shorten the diffusion path for electrons and lithium ions, which enhances the rate capability of NCM111 microrods [29].

2.3.2. Compositionally graded $LiNi_{0.5}Co_{0.2}Mn_{0.3}O_2$ micospheres.

$LiNi_{0.5}Co_{0.2}Mn_{0.3}O_2$ (NCM523) is a popular cathode composition whose increased Ni content significantly improves its capacity, in comparison with NCM111. However, due to the high reactivity of the increased amount of Ni^{4+} towards organic electrolyte, the cycling performance and especially the thermal stability are lowered, which

16
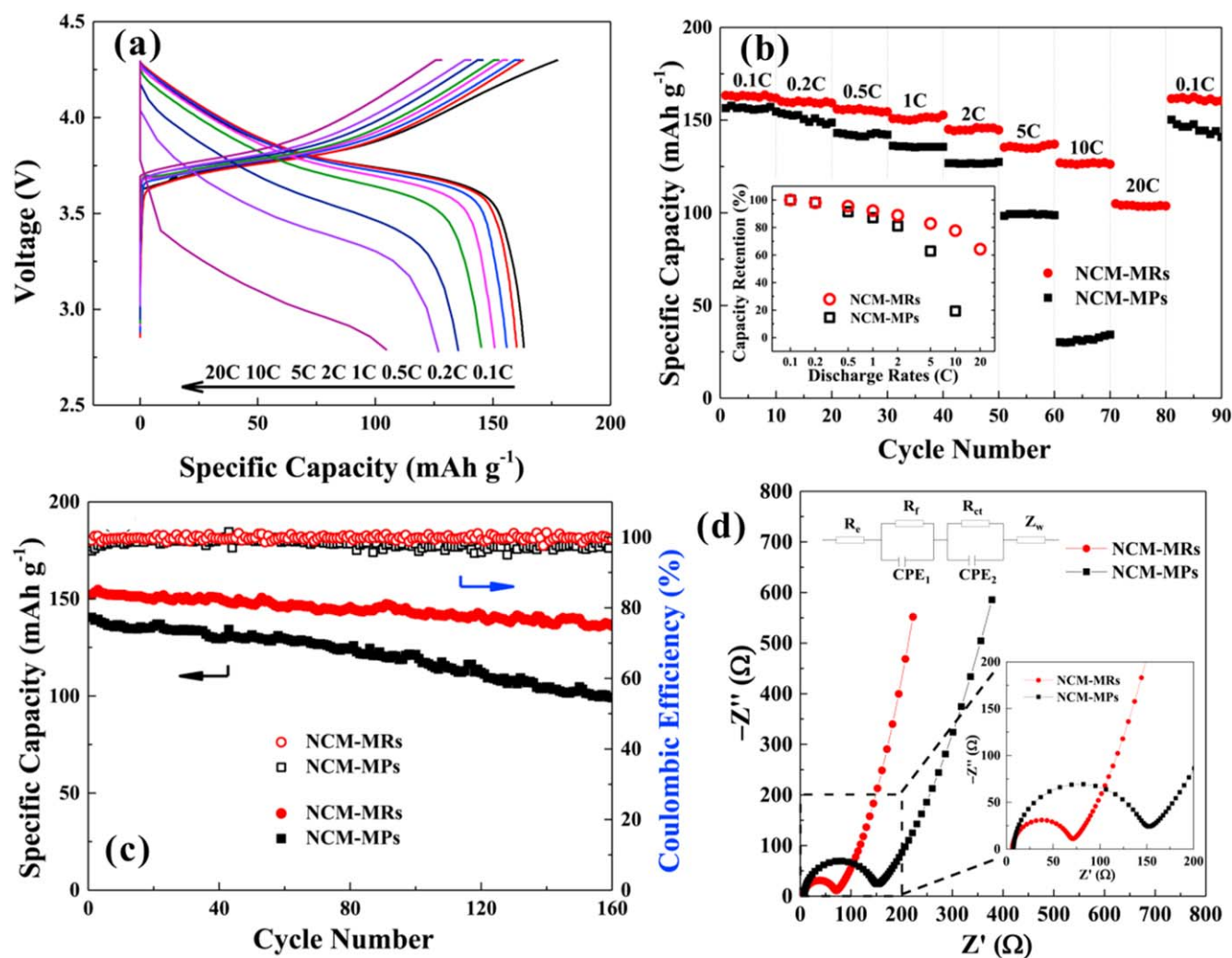
Figure 22. (a) The typical charge–discharge curves for NCM111 microrods; (b) rate capabilities, (c) cycling performances and (d) Nyquist plots for NCM111 microrods (denoted as NCM-MRs) and microparticles (denoted as NCM-MPs). Reprinted from [29], Copyright 2014, with permission from Elsevier.
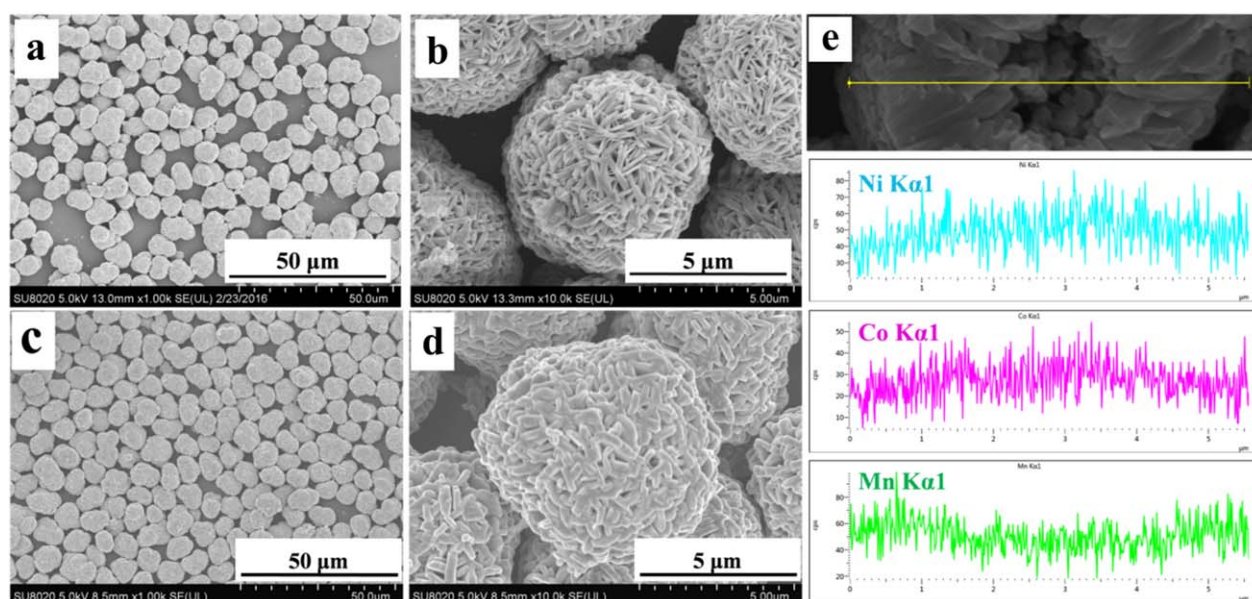
Figure 23. FESEM images of (a), (b) precursor and (c), (d) final product for NCM523 prepared via stepwise co-precipitation method; (e) cross-section line-scanning EDS spectra of a broken NCM523 particle. Reproduced with permission from [30].
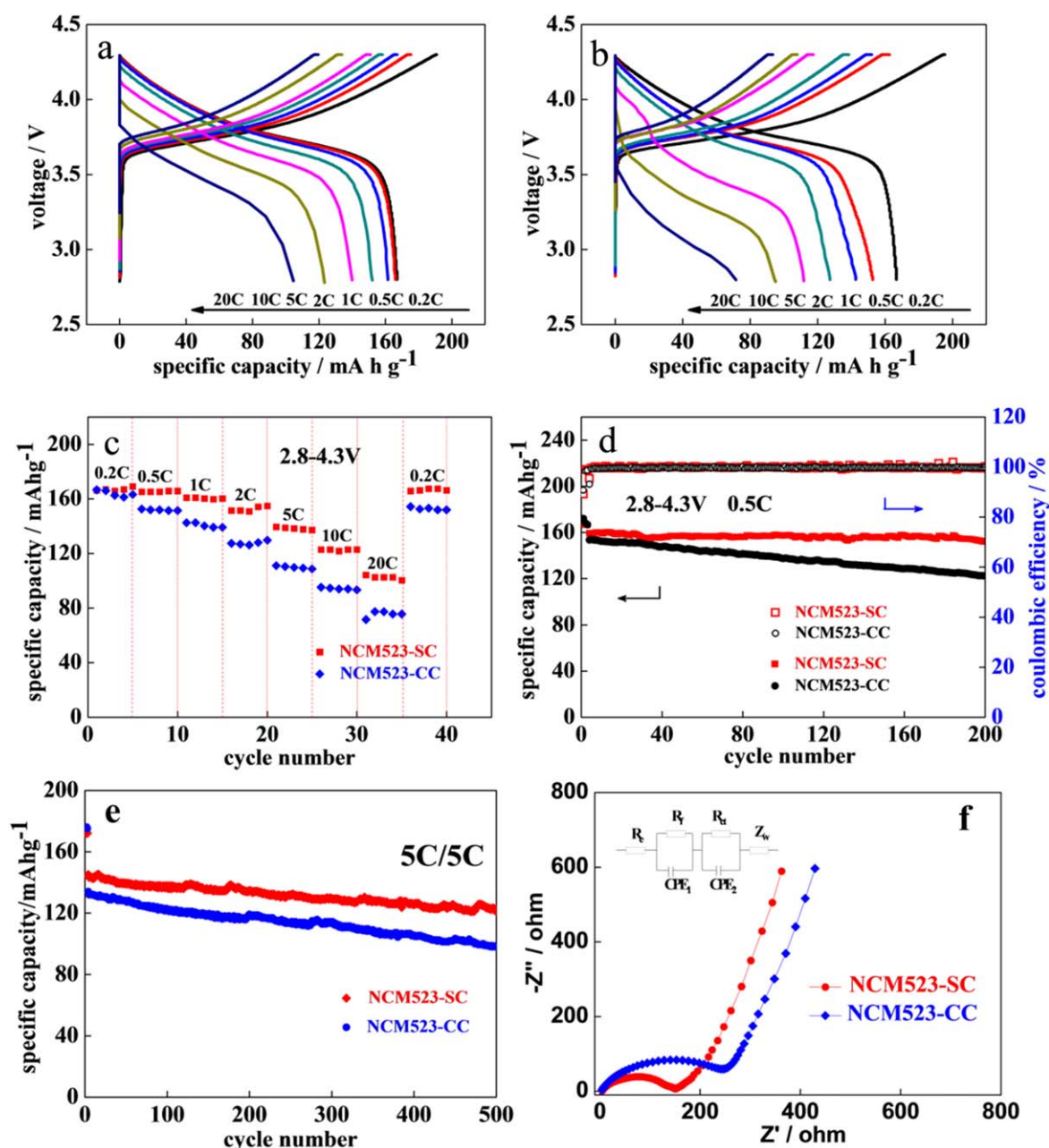
Figure 24. Charge–discharge curves of (a) NCM-SC and (b) NCM-CC; comparisons of (c) rate capability, (d) cycling performance at 0.5 C, (e) fast charge–discharge cycling performance at 5 C and (f) Nyquist plots for NCM-SC and NCM-CC. Reproduced with permission from [30].

mitigate its advantage of high capacity. To carry forward its high capacity and improve its poor structural stability, a concentration-gradient NCM523 cathode material consisting of Ni-rich core and Ni-poor outer shell via a simple stepwise precipitation strategy has been introduced [30].

The stepwise synthesis involves three sequential co-precipitation reactions of NaOH with the mixed solutions of $NiSO_4$, $CoSO_4$ and $MnSO_4$ with intentionally designed gradient Ni:Co:Mn ratios. The first solution (Ni:Co:Mn = 6:2:2) ensures the Ni-rich core of the finally product, while the second solution keeps the expected ratio of Ni:Co:Mn = 5:2:3. The last solution with Ni:Co:Mn = 4:2:4 significantly lowers the Ni content and

simultaneously increase the Mn concentration on the shell of NCM spheres, whereas the overall composition remains as $LiNi_{0.5}Co_{0.2}Mn_{0.3}O_2$ after the calcination with Li_2CO_3 [30].

The precursors for NCM523 prepared via the current stepwise precipitation method are in spherical shape with the size of about 8 μm, consisting of flake-like primary particles (figures 23(a), (b)). After thermal treatment, small flakes on the surface of NCM523 particles are slightly melted, without obvious changes of the morphology (figures 23(c), (d)). The primary flakes stack together to form rich diffusion paths for charge and ions. The line-scanning EDS spectra of a broken NCM523 particle have indicated that the Ni content is higher
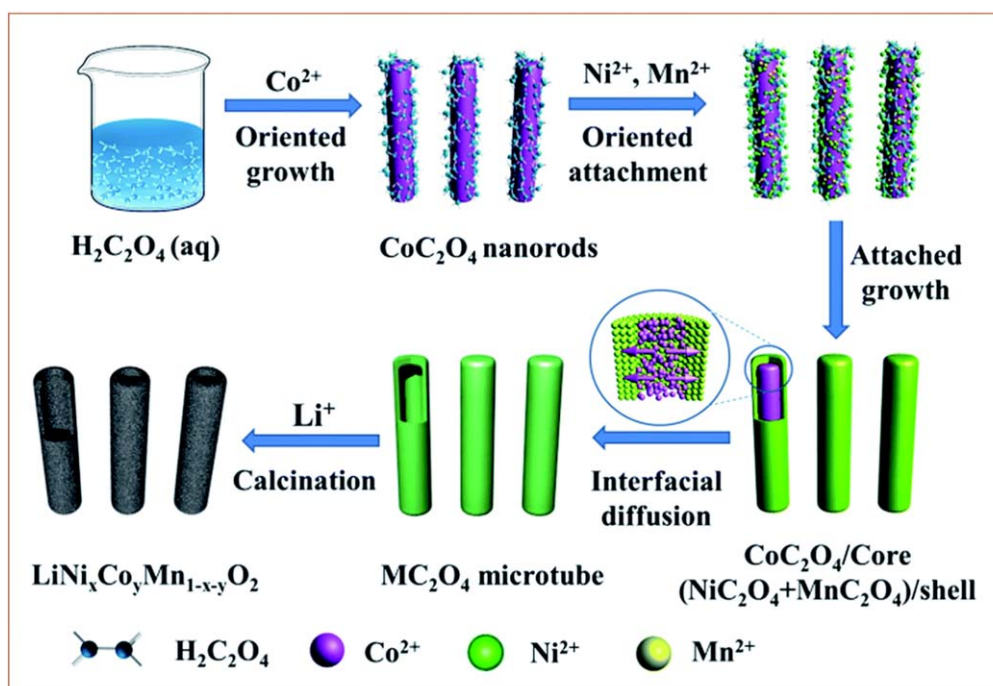
Figure 25. Illustration of sequential precipitation induced non-equilibrium interdiffusion, enabled by the design of a less crystalline and more loose core and a more compact crystalline shell, for the synthesis of ternary-metal oxalate $MC_2O_4 \cdot xH_2O$ (M= Ni, Co and Mn) microtubes and their conversion into $LiNi_xCo_yMn_{1-x-y}O_2$ microtubes through subsequent lithium implantation and calcination. Reproduced from [31] with permission from The Royal Society of Chemistry.
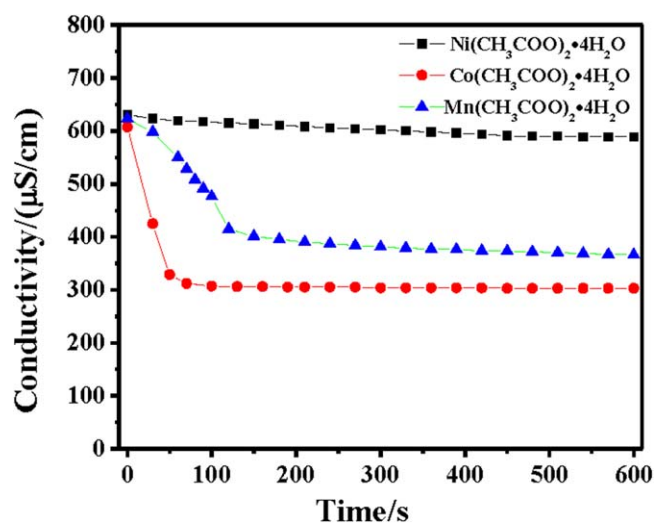

Figure 26. The variation of ionic conductivities for the solutions of $Mn(CH_3COO)_2 \cdot 4H_2O$, $Ni(CH_3COO)_2 \cdot 4H_2O$ and $Co(CH_3COO)_2 \cdot 4H_2O$ react with oxalic acid, respectively. Reproduced from [31] with permission from The Royal Society of Chemistry.

in the core center of the particle than in the outer shell, whereas the Mn content is more distributed in the shell than in the center (figure 23(e)), which strongly support the gradient-concentration microstructure of the sample as we designed.

To demonstrate the advantage of the current stepwise co-precipitation method, NCM523 materials without gradient concentration are prepared for comparison. The NCM samples with the same compositions are synthesized in a single batch of co-precipitation (denoted as NCM-CC), in comparison with the three steps of co-precipitation reactions (denoted as NCM-SC). The NCM-SC sample displays a discharge capacity of 166.3 mAh g^{-1}, comparable to that of NCM-CC (figures 24(a), (b)). However, at higher current rates, NCM-SC presents much higher capacity than NCM-CC, implying its superior rate performance (figure 24(c)).

The concentration-gradient NCM-SC material also shows much better cycling performance than NCM-CC, with the capacity retention of 95.8% after 200 charge–discharge cycles at 0.5 C (figure 24(d)). In contrast, the capacity retention of NCM-CC is only 79.6% under the same condition. Under the high charge/discharge rates (5 C), NCM-SC cathode displays a capacity of 121.9 mAh g^{-1} after 500 cycles, corresponding to the capacity fading of 0.3‰ per cycle, whereas NCM-CC sample has a much lower capacity of 98.2 mAh g^{-1} and a much higher fading rate of 0.54‰/cycle (figure 24(e)), implying the superior electrochemical performances for the fast charge–discharge applications such as EVs. The EIS test reveals that NCM-SC material has a substantially lower charge transfer resistance of about 150 Ω, in comparison with the resistance of 245.1 Ω for NCM-CC (figure 24(f)). The superior cycling performance of NCM-SC should be attributed to its concentration-gradient structure that reduces the possibility of side reactions and increases the structural stability during repeated electrochemical cycles. The porous and cross-linked structures in $LiNi_{0.5}Co_{0.2}Mn_{0.3}O_2$ material formed during thermal annealing process may facilitate the charge transfer and Li$^+$ diffusion, eventually improving the rate capability [30].
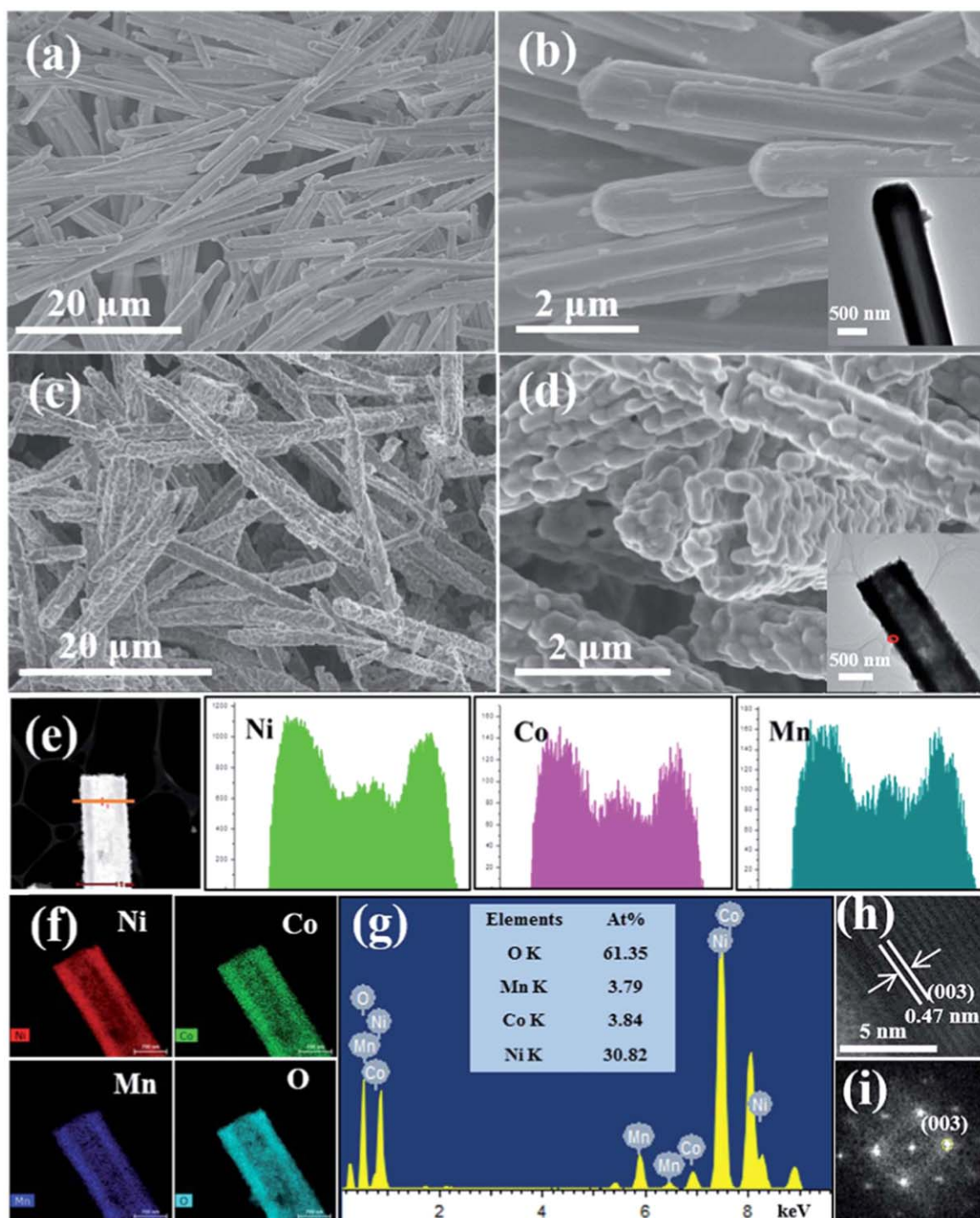
Figure 27. FESEM images of (a) and (b) the $MC_2O_4 \cdot xH_2O$ (M= Ni, Co and Mn) precursor for $LiNi_{0.8}Co_{0.1}Mn_{0.1}O_2$ and (c) and (d) the $LiNi_{0.8}Co_{0.1}Mn_{0.1}O_2$ product (inset in (b): high resolution TEM image of a microtube precursor with a reaction time of 8 h; inset in (d): high resolution TEM image of a microtube product); (e) EDS elemental line scans (Ni, Co, Mn) of a $LiNi_{0.8}Co_{0.1}Mn_{0.1}O_2$ microtube along the radial direction; (f) EDS elemental mappings (Ni, Co, Mn and O) and (g) EDS spectrum of the $LiNi_{0.8}Co_{0.1}Mn_{0.1}O_2$ microtube; (h) HRTEM image of the circled region of the inset in (d); (i) FFT pattern of the HRTEM image in (h). Reproduced from [31] with permission from The Royal Society of Chemistry.

2.3.3. $LiNi_{0.8}Co_{0.1}Mn_{0.1}O_2$ microtubes. Despite of their many intrinsic problems, including cation mixing, detrimental side reactions and thermal runaway issue, researchers are still keen on developing Ni-rich $LiNi_xCo_yMn_{1-x-y}O_2$ (Generally, $0.6 \leqslant x < 1$; $0 < y \leqslant 0.2$) cathode materials owing to the seduced high capacity of even higher than 200 mAh g^{-1} [3]. Part of the above problems can be remitted by e.g. cation doping to inhibit the diffusion of Ni^{2+} into Li^+ layer and surface coating to stabilize the solid-electrolyte interface [2, 7, 31]. Rational design of 1D hollow structured cathode
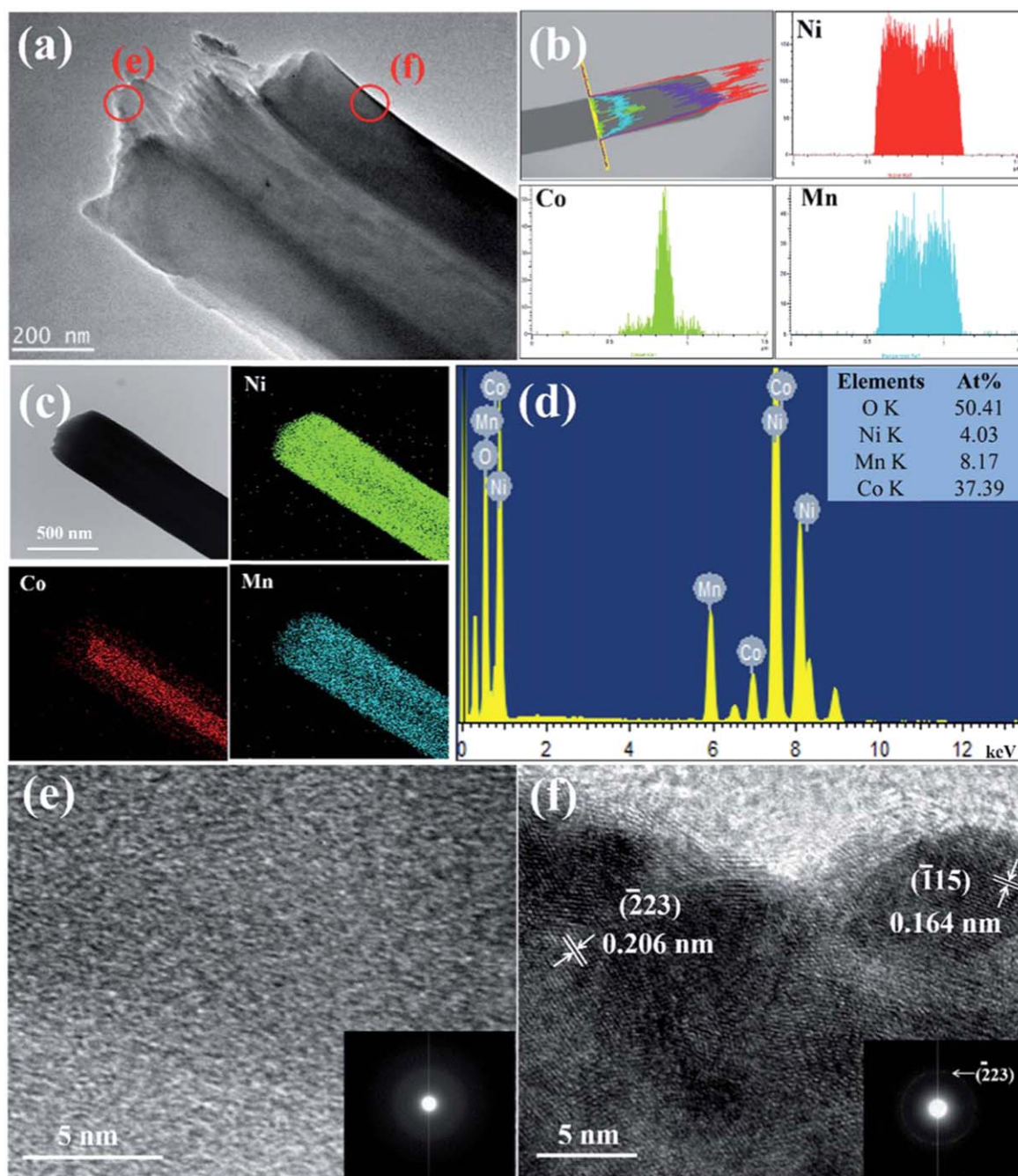
Figure 28. (a) High resolution TEM image of the core/shell structure of the $MC_2O_4 \cdot xH_2O$ (M = Ni, Co and Mn) precursor for $LiNi_{0.8}Co_{0.1}Mn_{0.1}O_2$ with a reaction time of 10 min (b) EDS elemental line scans of the $MC_2O_4 \cdot xH_2O$ (M = Ni, Co and Mn) core/shell precursor along the radial direction of the core/shell precursor. (c) Elemental mappings and (d) EDS spectrum of the core–shell structure precursor; (e) HRTEM image of the $CoC_2O_4 \cdot xH_2O$ core of the circled region, e, shown in (a) (inset in (e): the corresponding SAED pattern). (f) HRTEM image of the $MC_2O_4 \cdot xH_2O$ (M= Ni, Mn) shell of the circled region, f, shown in (a) (inset in (f): the corresponding SAED pattern). Reproduced from [31] with permission from The Royal Society of Chemistry.

materials emerges as an alternative but effective approach for solving the above issues, since the 1D structure can offer large contact areas and short Li^+ diffusion paths, while hollow structure can facilitate efficient electrode-electrolyte contact, reduce the diffusion path of Li^+ and accommodate the volume change during cycling process [31].

We have proposed a general and flexible strategy to synthesize $LiNi_{0.8}Co_{0.1}Mn_{0.1}O_2$ hollow microtubes. As illustrated in figure 25, in the sequential precipitation of ternary-

metal oxalate precursors, $CoC_2O_4 \cdot xH_2O$ was chosen to precipitate first to serve the following two purposes. One is to make use of its growth habit into nanorods which can template the oriented attachment growth of $NiC_2O_4 \cdot xH_2O$ and $MnC_2O_4 \cdot xH_2O$ precipitates in the subsequent co-precipitation. The other is to take advantage of the crystallinity difference between the initially formed $CoC_2O_4 \cdot xH_2O$ core and the subsequently formed $NiC_2O_4 \cdot xH_2O$ and $MnC_2O_4 \cdot xH_2O$ shell. It was found that the inner $CoC_2O_4 \cdot xH_2O$ core is less crystalline
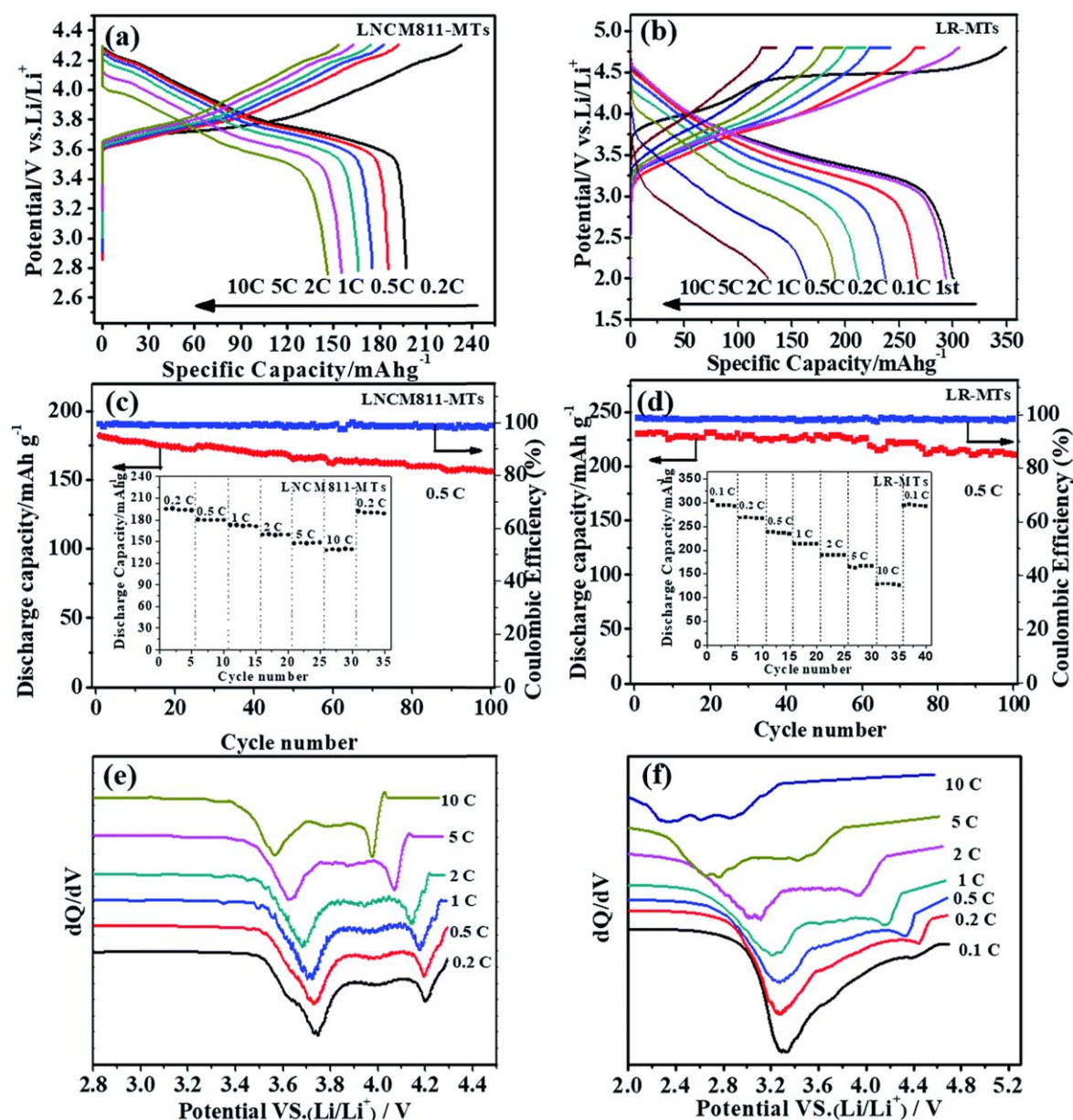
Figure 29. Typical charge–discharge curves for (a) $LiNi_{0.8}Co_{0.1}Mn_{0.1}O_2$ microtubes (denoted as LNCM811-MTs) and (b) $Li_{1.2}Ni_{0.13}Co_{0.13}Mn_{0.54}O_2$ microtubes (denoted as LR-MTs) at different discharge rates; cycling performances of (c) LNCM811-MTs and (d) LR-MTs at 0.5 C; inset in (c) and (d): rate cyclability at various rates; plots of dQ/dV of (e) LNCM811-MTs and (f) LRMTs at a rate of 0.1 C. Reproduced from [31] with permission from The Royal Society of Chemistry.

than the outer $NiC_2O_4 \cdot xH_2O$ and $MnC_2O_4 \cdot xH_2O$ shell due to the faster nucleation and growth kinetics of the former in a much more saturated solution when first precipitated [31].

It should be noted that the reaction kinetics are at play for the formation of the tube-like microstructures rather than the thermodynamics, since the solubility product constant follows the order: $MnC_2O_4 \cdot 2H_2O$ (1.7×10^{-7}) > $CoC_2O_4 \cdot 4H_2O$ (6.3×10^{-8}) > $NiC_2O_4 \cdot 2H_2O$ (4×10^{-10}). The variations of the ionic conductivity indicate that $CoC_2O_4 \cdot 4H_2O$ displays the highest precipitation rate (figure 26), whereas $NiC_2O_4 \cdot 2H_2O$ has the lowest. $CoC_2O_4 \cdot 4H_2O$ thus has a faster nucleation rate than the other two, accounting for the formation of smaller and less crystalline $CoC_2O_4 \cdot 4H_2O$ primary particles. The crystallinity difference between the

core and shell is the main driving force for the non-equilibrium mass interdiffusion during ripening process, which causes net outward mass transfer from the loose and poorly crystalline core and opens the inner space due to the Kelvin effect (figure 25). The mass gain on the concave surface is at the expense of the mass loss on the convex surface. Eventually, the ternary-metal oxalate $MC_2O_4 \cdot xH_2O$ (M = Ni, Co and Mn) microrods with core–shell structure turn into hollow microtubes, which transform into $LiNi_{0.8}Co_{0.1}Mn_{0.1}O_2$ (NCM811) microtubes after lithium impregnation and thermal annealing [31].

The obtained $MC_2O_4 \cdot xH_2O$ (M = Ni, Co and Mn) precursors show the tube-like morphology with the diameters of about 1 μm and lengths of about 20 μm (figures 27(a), (b)).
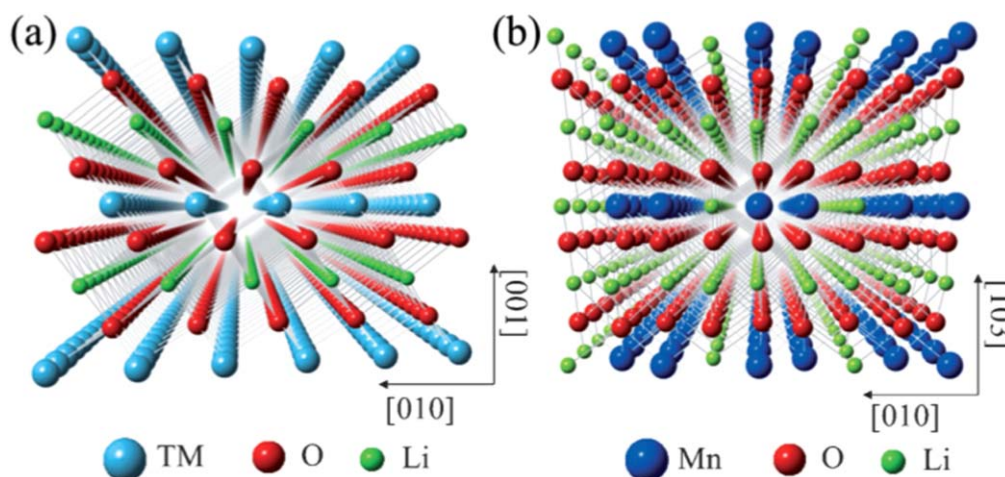
Figure 30. Crystal structures of (a) the rhobohedral LiTMO$_2$ (space group: $R\bar{3}m$, TM= Ni, Co and Mn) and (b) monoclinic Li$_2$MnO$_3$ (space group: C/2m) viewed from the [100] crystallographic direction. [36] John Wiley & Sons. Copyright © 2013 WILEY-VCH Verlag GmbH & Co. KGaA, Weinheim.
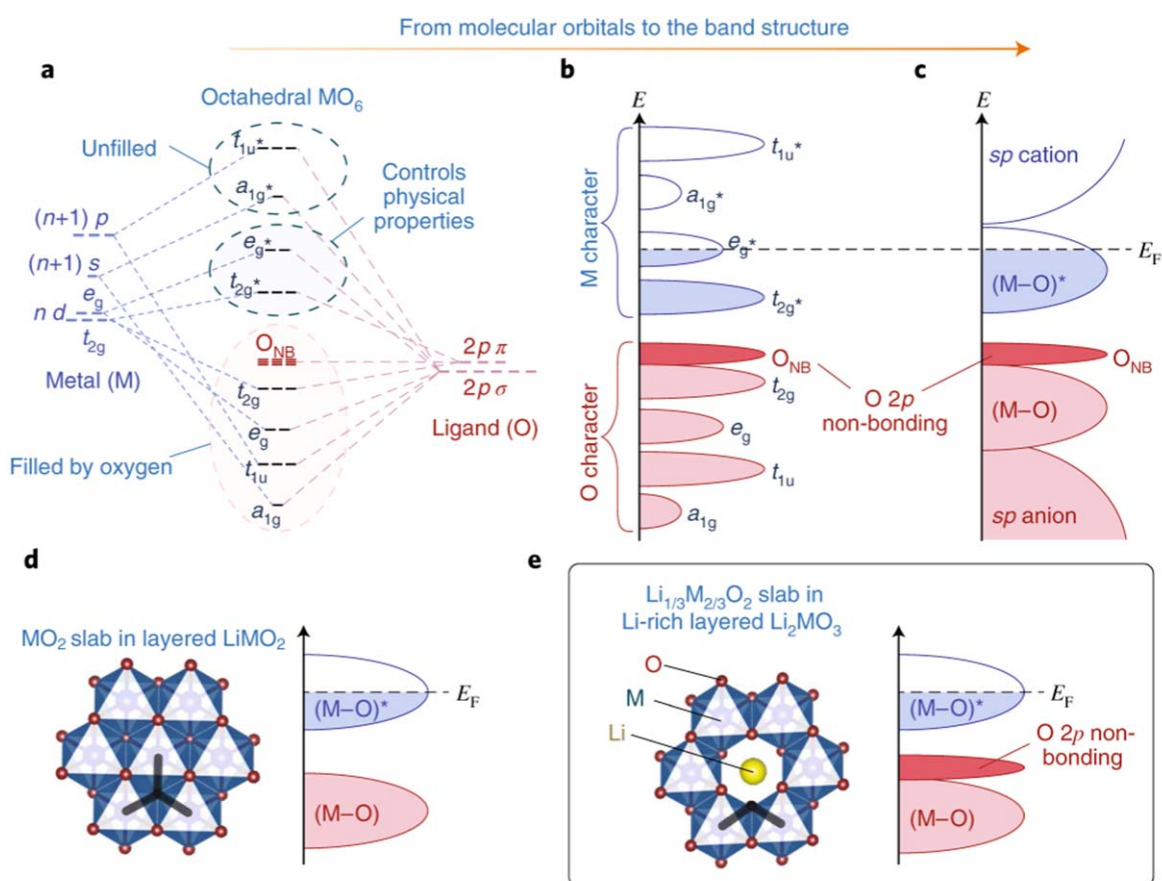
Figure 31. Band structure of oxides and the anionic redox mechanism. As depicted by a to c, the schematic band structure of (c) transition-metal oxides can be built by extrapolating the molecular orbital energy diagram for (a) octahedral MO$_6$. ONB denotes the O 2p non-bonding states located below the anti-bonding (M–O)* band and just above the bonding (M–O) band. A comparison of (d) LiMO$_2$ and (e) Li-rich Li$_2$MO$_3$, in terms of their crystal structures (focusing on slabs of MO$_2$ or Li$_{1/3}$M$_{2/3}$O$_2$) and the relevant parts of their band structures, reveals how the two structures differ in oxygen coordination. Thick black lines highlight three M neighbors for each O in (d) LiMO$_2$, compared with only two in the honeycomb-arranged (e) Li$_2$MO$_3$, thus giving rise to O 2p non-bonding states in the latter. Note that these are schematic band structures without taking into account the electron-electron correlations. Reprinted by permission from Springer Nature Customer Service Centre GmbH: Springer Nature, Nature Energy [38] 2018.
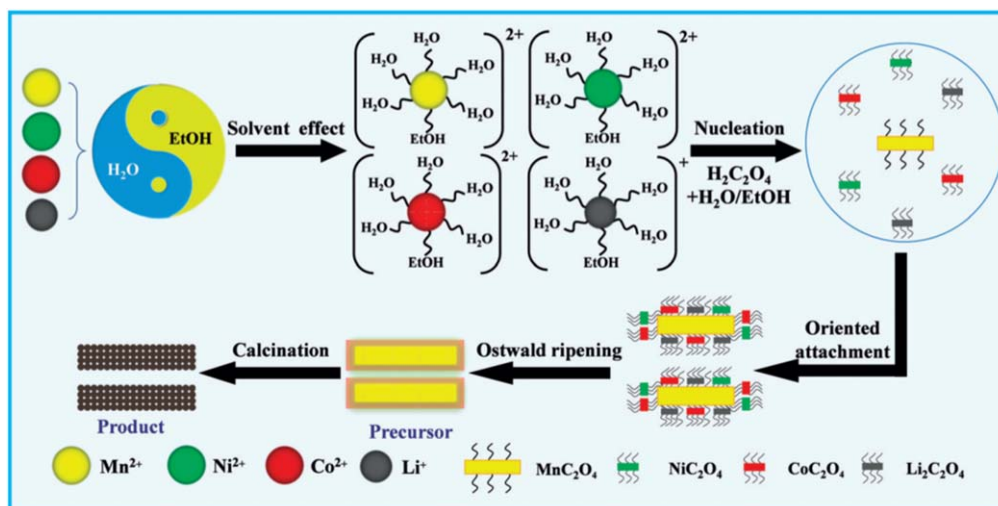
Figure 32. Schematic illustration of ethanol mediated co-precipitation coupled with subsequent calcination for the formation of $0.5Li_2MnO_3 \cdot 0.5LiNi_{1/3}Co_{1/3}Mn_{1/3}O_2$ 1D porous micro- and nanostructured bars. [40] John Wiley & Sons. © 2016 WILEY-VCH Verlag GmbH & Co. KGaA, Weinheim.

The tubular architectures are well maintained after transformation into NCM811 product (figures 27(c), (d)), except that the surface becomes coarse and the tips of the tube are opened, probably due to the large strain during the thermal annealing process. Different characterization techniques further confirm the 1D micro-tubular structure of the NCM811 product synthesized by the current strategy.

During the second-step co-precipitation of nickel and manganese oxalates for 10 min, the coaxial core/shell structured metal oxalate precursor can be clearly observed (figure 28(a)). The EDS line scans and elemental mappings clearly show that Co element is mainly distributed in the core of the tube, while Ni and Mn elements stay on the shell (figures 28(b), (c)). The HRTEM images and SAED patterns focusing on the core and shell of the tubular $MC_2O_4 \cdot xH_2O$ (M = Ni, Co and Mn) precursor display a significant difference. The $CoC_2O_4 \cdot xH_2O$ core exhibit the amorphous characteristics at the atomic scale (figure 28(e)), while the $MC_2O_4 \cdot xH_2O$ (M = Ni, Mn) shell presents the lattice fringes and electron diffraction ring pattern of $NiC_2O_4 \cdot xH_2O$, which is a strong support for our designed synthetic strategy.

The unique microstructures offer the cathode materials great electrochemical performances. For instance, the initial discharge capacity of NCM811 microtubes can reach $194.5 \, mAh \, g^{-1}$ at the current rate of 0.2 C, with the initial coulombic efficiency of 83.3% (figure 29(a)). In contrast, the initial discharge capacity and coulombic efficiency of NCM811 microparticles at 0.2 C are only $188.5 \, mAh \, g^{-1}$ and 82.6%, respectively. The capacity retention of NCM811 microtubes is as high as 87.4% after 100 cycles at 0.5 C (figure 29(c)), which is also significantly than that of NCM811 microparticles (75.6%). The cycling performance and rate capability of the tubular NCM811 cathodes are all superior to the particulate counterparts. The enhanced electrochemical performances of NCM811 microtubes should be due to their special 1D and hollow structures that are beneficial for the lowered polarization (figure 29(e)). The unique structures not only enhance the

contact between the active material and electrolyte, but also facilitate the charge and ion transfers, synergistically contributing to their superior electrochemical properties that might be further improved through surface coating by e.g. γ-$LiAlO_2$ and other compositions [9, 32].

2.4. Li-rich layered oxides

The experimental work about Li-rich layered oxide can be dated back to early in 1990s when Thackeray and coworkers reported the synthesis of $Li_{1.09}Mn_{0.91}O_2$ from Li_2MnO_3 by acid digestion [33, 34]. The chemical compositions of Li-rich layered oxides are commonly written in several expressions, e.g. $xLi_2MnO_3(1-x)LiMO_2$ and $Li_{1+x}M_{1-x}O_2$ (M = Ni, Co, Mn etc), which can be easily converted to each other [2]. As implied by the composition of $xLi_2MnO_3(1-x)LiMO_2$, the crystal structure of can be regarded as the composite of the monoclinic Li_2MnO_3 (Space group: C2/m) and rhombohedral $LiMO_2$ (Space group: $R\bar{3}m$). Both of them have a layered structure, sharing strong similarity [2, 34, 35].

As shown in figure 30(a), the layered rhombohedral $LiMO_2$ (or written as $LiTMO_2$) (M/TM= Ni, Co, Mn etc) adopts the alternative stacking sequence of …–Li–O–M–O–Li–… along the c axis. The structure is very similar to the structure of monoclinic Li_2MnO_3, except that the Mn layers are mixed with Li atoms in the Li/Mn ratio of 1/2 (figure 30(b)). The structural similarity can be easily understood by converting the formula of Li_2MnO_3 into $Li[Li_{1/3}Mn_{2/3}]O_2$ [36]. The ordered arrangement of Li^+ in Mn^{4+} layer significantly reduces the symmetry from $R\bar{3}m$ to C2/m.

Due to their very similar structures, there exists another understanding that Li-rich layered oxide is a homogeneous solid solution of these two components, as represented by the formula of $Li_{1+x}M_{1-x}O_2$ [2, 34]. The structural differentiation of Li-rich layered cathode materials is commonly accomplished by XRD to observe the few representative but very weak diffraction peaks within the 20°–25° range caused by the Li^+/Mn^{4+} ordered superstructure, but unfortunately,
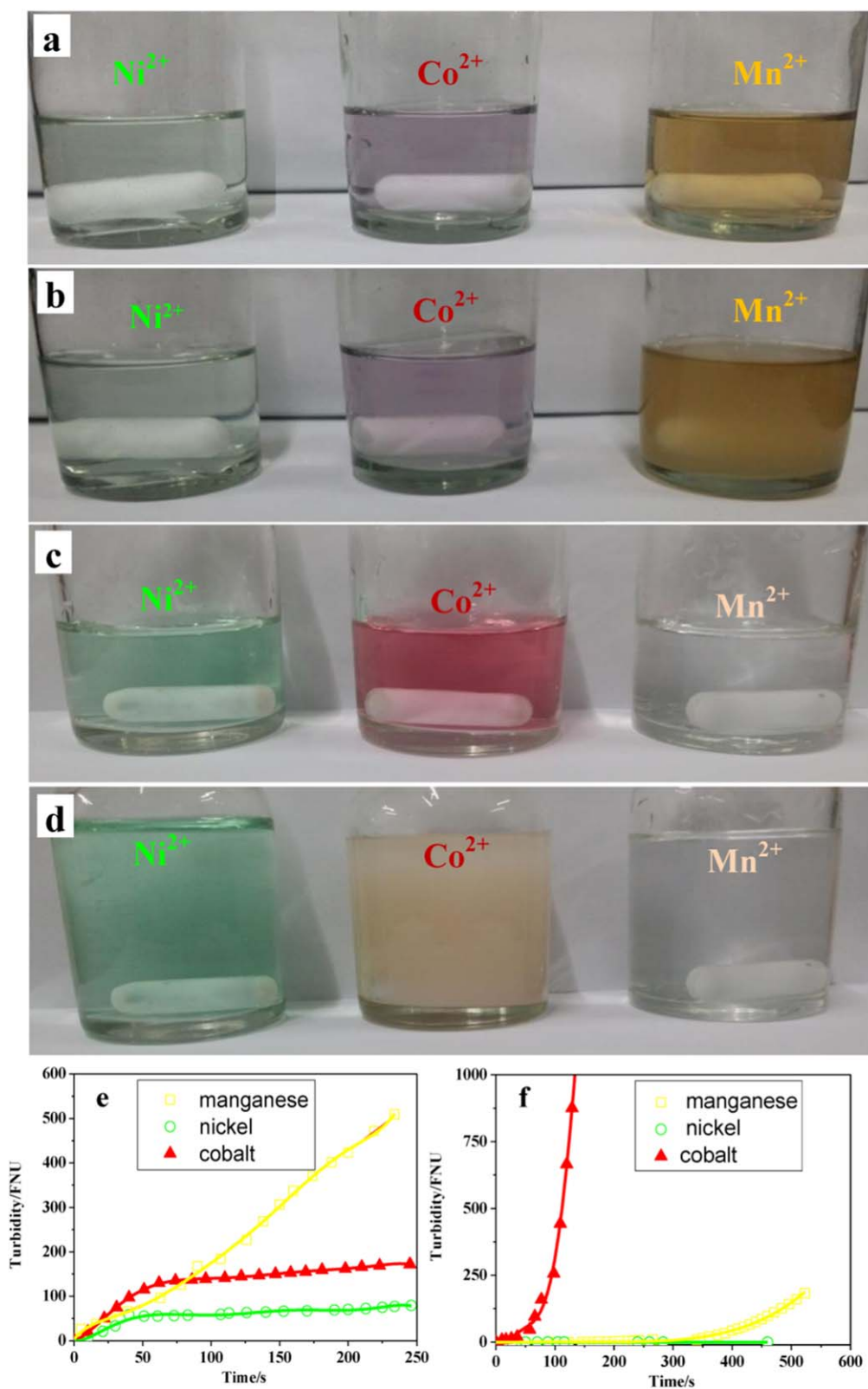
Figure 33. Optical images of Ni^{2+}, Co^{2+} and Mn^{2+} solutions in (a), (b) ethanol-water mixed solvent and (c), (d) pure water solvent at different co-precipitation reaction stages: (a), (c) before and (b), (d) right after the reaction with oxalic acid; turbidity changes of each solution versus time when co-precipitation reactions occurring (e) in ethanol/water mixed solvent, (f) in pure water. Ethanol/water ratio R = 5:1. [40] John Wiley & Sons. © 2016 WILEY-VCH Verlag GmbH & Co. KGaA, Weinheim.
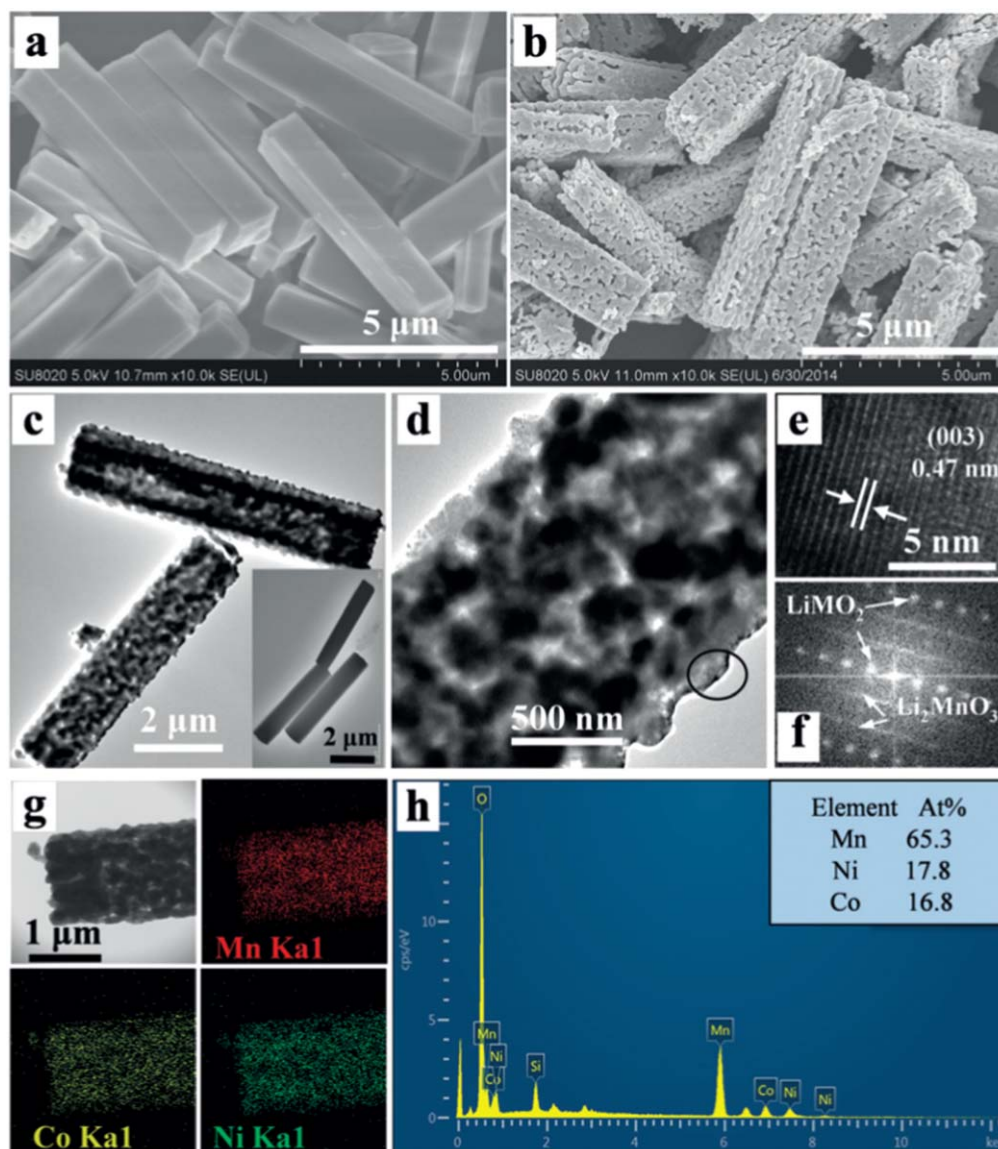
Figure 34. FESEM images of (a) $MC_2O_4 \cdot xH_2O$ (M = Mn, Ni, Co, Li) precursor and (b) $0.5Li_2MnO_3 \cdot 0.5LiNi_{1/3}Co_{1/3}Mn_{1/3}O_2$ product; (c), (d) TEM and HRTEM images of the product (inset of c: TEM image of precursor); (e) HRTEM image of the circled region in (d); (f) FFT of the HRTEM image in (e); (g) elemental mapping and (h) EDS spectrum of the tip of a $0.5Li_2MnO_3 \cdot 0.5LiNi_{1/3}Co_{1/3}Mn_{1/3}O_2$ microbar (R = 5:1). [40] John Wiley & Sons. © 2016 WILEY-VCH Verlag GmbH & Co. KGaA, Weinheim.

XRD only gives the average crystal structure. Deep understanding on the local structures in Li-rich layered oxides requires combined advanced characterization techniques, such as synchrotron x-ray diffraction, high angle annular dark field scanning transmission electron microscopy, neutron diffraction, etc Interested readers are advised to find the detailed interpretation of the local structure in Li-rich layered oxides in many articles and review papers [2, 34–37].

The most striking advantage of Li-rich layered oxides is their exceptionally high capacity of about $300 \, \text{mAh g}^{-1}$, overwhelming all the currently available commercial LIB cathodes. The exact mechanism behind the high charge/discharge capacities of Li-rich layered oxides is complicated. However, two main contributions are well recognized. Take charge capacity as the example. One contribution is from the active oxidation of M^{3+} to M^{4+}, when the battery is charged

up to about 4.4 V. The other is the oxidation of O^{2-} occurring at higher charging voltage, as reflected by the long plateau above 4.4 V, accounting for about half of the overall discharge capacity of Li-rich layered oxides. The latter contribution is well known as the anionic redox mechanism.

From the molecular orbital point of view, the nd, $(n + 1) s$ and $(n + 1) p$ orbitals of center metal M in octahedral MO_6 are overlapping with the s orbitals of six ligands (O) to give the σ molecular orbitals of the bonding states of a_{1g}, t_{1u} and e_g and the anti-bonding states of e_g^*, a_{1g}^* and t_{1u}^* (figure 31(a)) [38]. The t_{2g} orbitals of M interact with the p orbitals of ligands to form the π molecular orbitals of the bonding state of t_{2g} and anti-bonding state of t_{2g}^*. This gives rise to the completely filled bonding states and the partially filled anti-bonding states, where the ligand and center M characters dominate, respectively (figure 32(b)). In the periodic solid materials, the anti-bonding
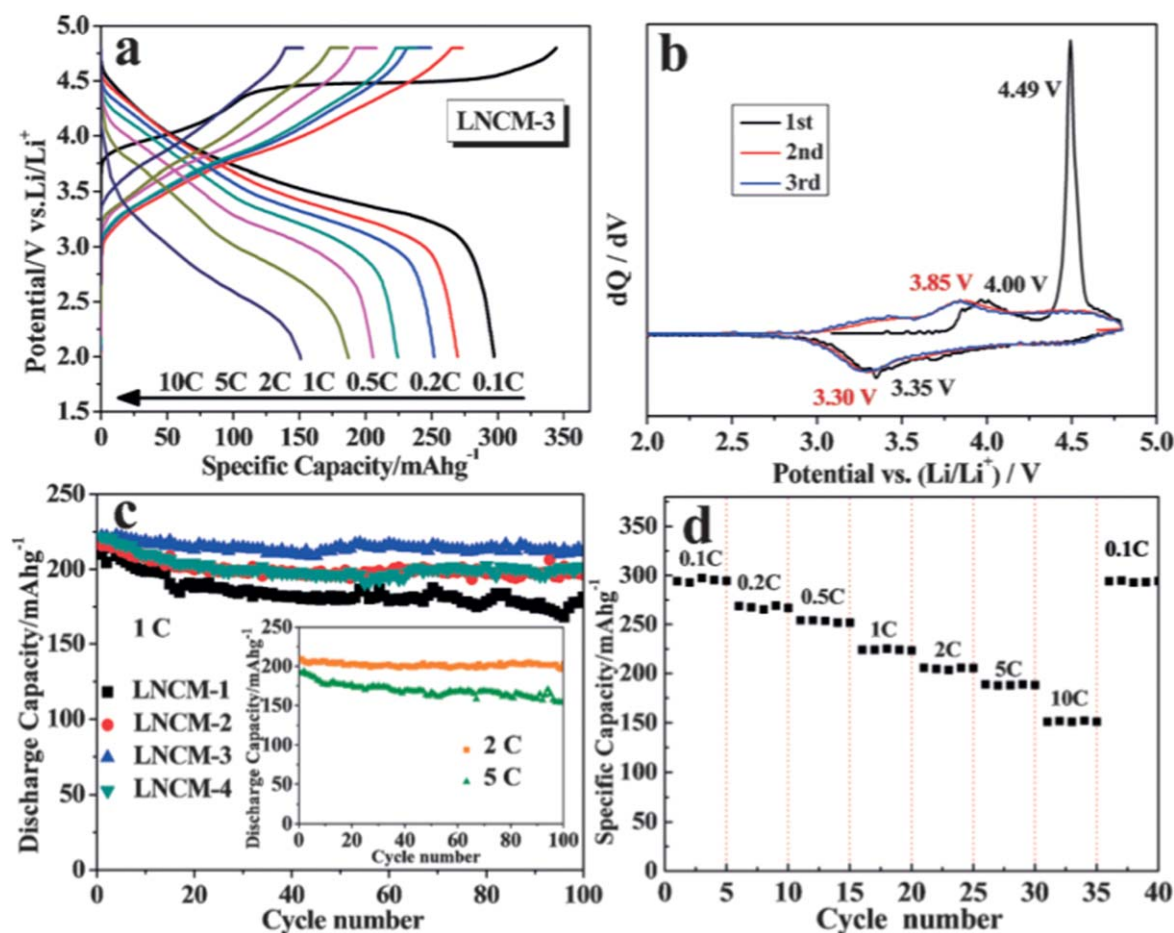
Figure 35. $0.5Li_2MnO_3 \cdot 0.5LiNi_{1/3}Co_{1/3}Mn_{1/3}O_2$ electrochemical performance (LNCM-3, $R = 5:1$) as an LIB cathode material: (a) charge–discharge profiles at various rates (2.0–4.8 V); (b) differential capacity dQ/dV (Q: capacity; V: voltage of the cells) plots at the rate of 0.1 C; (c) cycling performances in comparison with the other three samples at the rate of 1 C (inset: cycling performances of LNCM-3 at 2 C and 5 C); (d) rate capability of LNCM-3 at different rates (1 C = 250 mAh g^{-1}). [40] John Wiley & Sons. © 2016 WILEY-VCH Verlag GmbH & Co. KGaA, Weinheim.

e_g^* and t_{2g}^* states become the continuous $(M–O)^*$ band that controls the electrochemistry of the materials (figure 32(c)). In the classical $LiMO_2$ layered oxides, all the 2p orbitals of the ligand O engage in M–O bond formation, for which the electrochemical charging reaction comes from the loss of electrons in $(M–O)^*$ band (or commonly called as d band) (figure 32(d)). However, in Li_2MnO_3-type Li-rich layered oxides (written as $Li[Li_{1/3}M_{2/3}]O_2$), one of the O 2p orbitals is weakly bonded because of its relatively small overlapping with Li 2s orbital. It thus behaves like an O non-bonding state and is located above the filled (M–O) bonding band (figures 32(c), (e)) [38]. Therefore, the oxygen redox is triggered as soon as the Fermi level is pinned at the top of O 2p states after the completion of M^{3+}/M^{4+} redox reactions. Interested readers can also find the details of anionic redox mechanism in many recent review articles [2, 38, 39].

Despite the exceptionally high capacity, there are many intrinsic issues to be conquered for the application of Li-rich layered oxide cathode materials, e.g. the large irreversible capacity loss in the initial cycle, fast capacity fading and voltage decay [2, 34]. These problems share more or less common reasons. For instance, the anionic oxidation during the first

charging process leads to the loss of Li_2O that cannot be completely inserted back to the host structure in the subsequent discharging process, which causes large irreversible capacity loss in the initial cycle. The anionic redox reaction also leaves large amounts of oxygen vacancies and Li vacancies in both the transition metal and Li layers, which induce the migration of TM cations into the Li vacancies. This inevitably causes the structural transition from layered to spinel-like phase, accelerating the capacity fading and voltage decay [2, 34, 35].

2.4.1. $0.5Li_2MnO_3 \bullet 0.5LiNi_{1/3}Co_{1/3}Mn_{1/3}O_2$ microbars and other cathodes.
$0.5Li_2MnO_3 \cdot 0.5LiNi_{1/3}Co_{1/3}Mn_{1/3}O_2$ is a typical example of Li_2MnO_3-type Li-rich layered metal oxide cathode material, which has undergone a flurry of research because of its high energy density. The construction of its 1D microstructure can well unlock its full potential as the high energy density cathode material, due to the shortening of electron and lithium diffusion paths, an appropriate contact area between the cathode and electrolyte, and the ability to accommodate the structural strain during charging/discharging reactions [40].

We have proposed a facile, general and mild approach for fabricating 1D micro- and nanostructured $0.5Li_2MnO_3 \cdot$
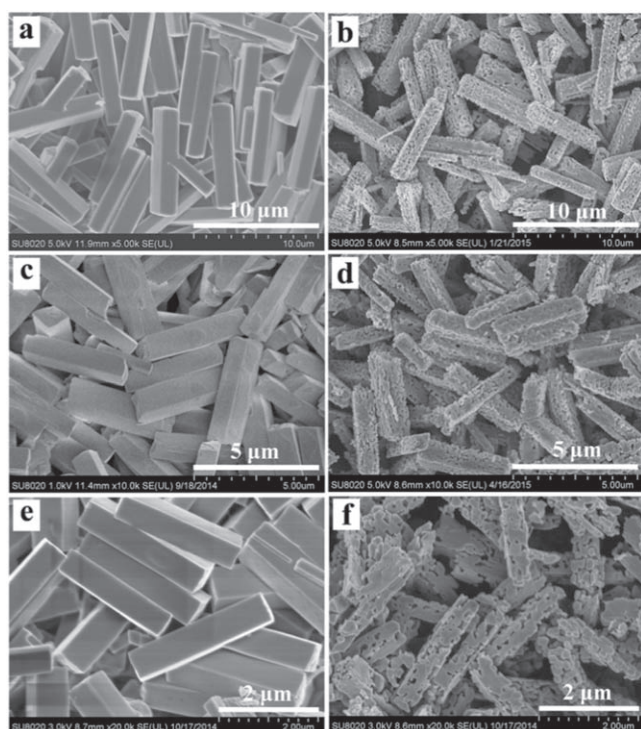
Figure 36. FESEM images of microbars: (a) precursor and (b) product of layered $0.5Li_2MnO_3 \cdot 0.5LiNi_{0.5}Mn_{0.5}O_2$; (c) precursor and (d) product of layered $LiNi_{1/3}Co_{1/3}Mn_{1/3}O_2$; (e) precursor and (f) product of spinel $LiNi_{0.5}Mn_{1.5}O_4$. [40] John Wiley & Sons. © 2016 WILEY-VCH Verlag GmbH & Co. KGaA, Weinheim.

$0.5LiNi_{1/3}Co_{1/3}Mn_{1/3}O_2$ material, by judiciously formulating the precipitating solvent [40]. The synthesis involves a co-precipitation step mediated by the mixed solvent of ethanol and water. Only under a certain ratio of ethanol-water in the mixed solvent, the uniform metal oxalate microbars $MC_2O_4 \cdot 2H_2O$ (M = Ni, Co, Mn) can be obtained (figure 32) via the co-precipitation reaction which undergoes at room temperature without use of any surfactant. The MnC_2O_4 nanobar seeds serve as templates for recruiting and assimilating other metal oxalates by oriented attachment and Ostwald ripening, yielding $MC_2O_4 \cdot 2H_2O$ microbars, which transform into $0.5Li_2MnO_3 \cdot 0.5LiNi_{1/3}Co_{1/3}Mn_{1/3}O_2$ 1D microbars upon thermal annealing (figure 32).

The use of the ethanol-water mixed solvent during synthesis capitalizes on the composition-dependent change in the dielectric constant and solvation power, which would have the impact on supersaturation degree and kinetics. The addition of ethanol into water reduces the dielectric constant and alters the solute-solvent interactions, thereby adjusting the relative order of reaction kinetics for Ni, Co and Mn, and their supersaturation degree, which may lower the nucleation barrier and thus facilitate co-precipitation. Comparison experiments demonstrate that Co^{2+} ions have the faster nucleation and growth kinetics with pure water as solvent (figures 33(c), (d)). In contrast, the nucleation and growth kinetics are altered in the ethanol-water mixed solvent, in which Mn^{2+} ions have the largest (figures 33(a), (b)). The comparison is more obvious by monitoring the variation of the turbidity for the different precipitation reactions. As

shown in figure 33(f), the turbidity for Co^{2+} precipitation occurring in pure water rises dramatically versus time. However, the kinetics of Mn^{2+} is more dominant when using ethanol/water mixed solvent (figure 33(e)). This strongly supports our proposed reaction mechanism.

The $MC_2O_4 \cdot 2H_2O$ precursor shows the rectangular bar-like architectures with the lengths of about 6.4 μm and widths of about 1.2 μm (figure 34(a)). The 1D bar-like structure has been well retained after heat treatment of the precursors, except that the $0.5Li_2MnO_3 \cdot 0.5LiNi_{1/3}Co_{1/3}Mn_{1/3}O_2$ microbars have plenty of porosity (figures 34(b)–(d)). The HRTEM image and FFT pattern (figures 34(e), (f)) strongly suggest that the as-prepared product is composed of a layered $LiNi_{1/3}Co_{1/3}Mn_{1/3}O_2$ (space group of $R\bar{3}m$) and the Li_2MnO_3 component (space group of C/2 m), with the uniform distribution of cations in the designed ratio (figures 34(g), (h)).

The electrochemical measurements have indicated that the Li-rich layered oxide of $0.5Li_2MnO_3 \cdot 0.5LiNi_{1/3}Co_{1/3}Mn_{1/3}O_2$ microbars prepared at the ethanol/water ratio of 5/1 (denoted as LNCM-3) has the best electrochemical performances, including, such as a high initial discharge capacity of 297.1 mAh g^{-1} and high coulombic efficiency of 86.4% at 0.1 C (figure 35(a)). Its discharge capacities are 211.4 and 202.8 mAh g^{-1} after 100 cycles at 1 C and 2 C respectively, corresponding to the high capacity retentions of 95% and 97% respectively (figure 35(c)), implying the good cycling performance of LNCM-3. In contrast, the Li-rich layered oxides prepared with other ethanol/water ratios, e.g. 0/1 (LNCM-1), 3/1 (LNCM-2) and 24/1 (LNCM-4), have much lower cycling performances (figure 35(c)). The $0.5Li_2MnO_3 \cdot 0.5LiNi_{1/3}Co_{1/3}Mn_{1/3}O_2$ microbars (LNCM-3) have also shown a good rate capability (figure 35(d)). The superior electrochemical performances of $0.5Li_2MnO_3 \cdot 0.5LiNi_{1/3}Co_{1/3}Mn_{1/3}O_2$ microbars should be resulted from their unique 1D porous architecture which has the advantages, such as shortening the electron and lithium diffusion lengths, facilitating efficient diffusion of electrolyte into the inner regions of the cathode, etc [40]. The current ethanol mediated co-precipitation coupled with subsequent post-heat treatment can be readily extended to other electrode materials with uniform 1D porous micro- and nanostructured bar-shape microstructures, including Li-rich $0.5Li_2MnO_3 \cdot 0.5LiNi_{0.5}Mn_{0.5}O_2$, spinel $LiNi_{0.5}Mn_{1.5}O_4$ and many others (figure 36).

2.4.2. $0.5Li_2MnO_3 \bullet 0.5LiNi_{1/3}Co_{1/3}Mn_{1/3}O_2$ microtubes. The hollow-tube structure of Li-rich layered oxide $0.5Li_2MnO_3 \cdot 0.5LiNi_{1/3}Co_{1/3}Mn_{1/3}O_2$ (alternatively written as $Li_{1.2}Ni_{0.13}Co_{0.13}Mn_{0.54}O_2$) can also be designed via the above-mentioned sequential precipitation strategy discussed in section 2.3.3. As illustrated in figure 25, our strategy is based on the non-equilibrium interdiffusion driven by the crystalline differences of the amorphous core and crystalline shell. Given adequate reaction time, the tube-like oxalate precursor with diameters of 1–2 μm and lengths of 10–20 μm can be readily obtained (figures 37(a)–(c)). The tube-like morphology of the oxalate precursor is largely kept after its transformation into $Li_{1.2}Ni_{0.13}Co_{0.13}Mn_{0.54}O_2$ microtubes (figures 37(d)–(f)). The $Li_{1.2}Ni_{0.13}Co_{0.13}Mn_{0.54}O_2$ microtubes
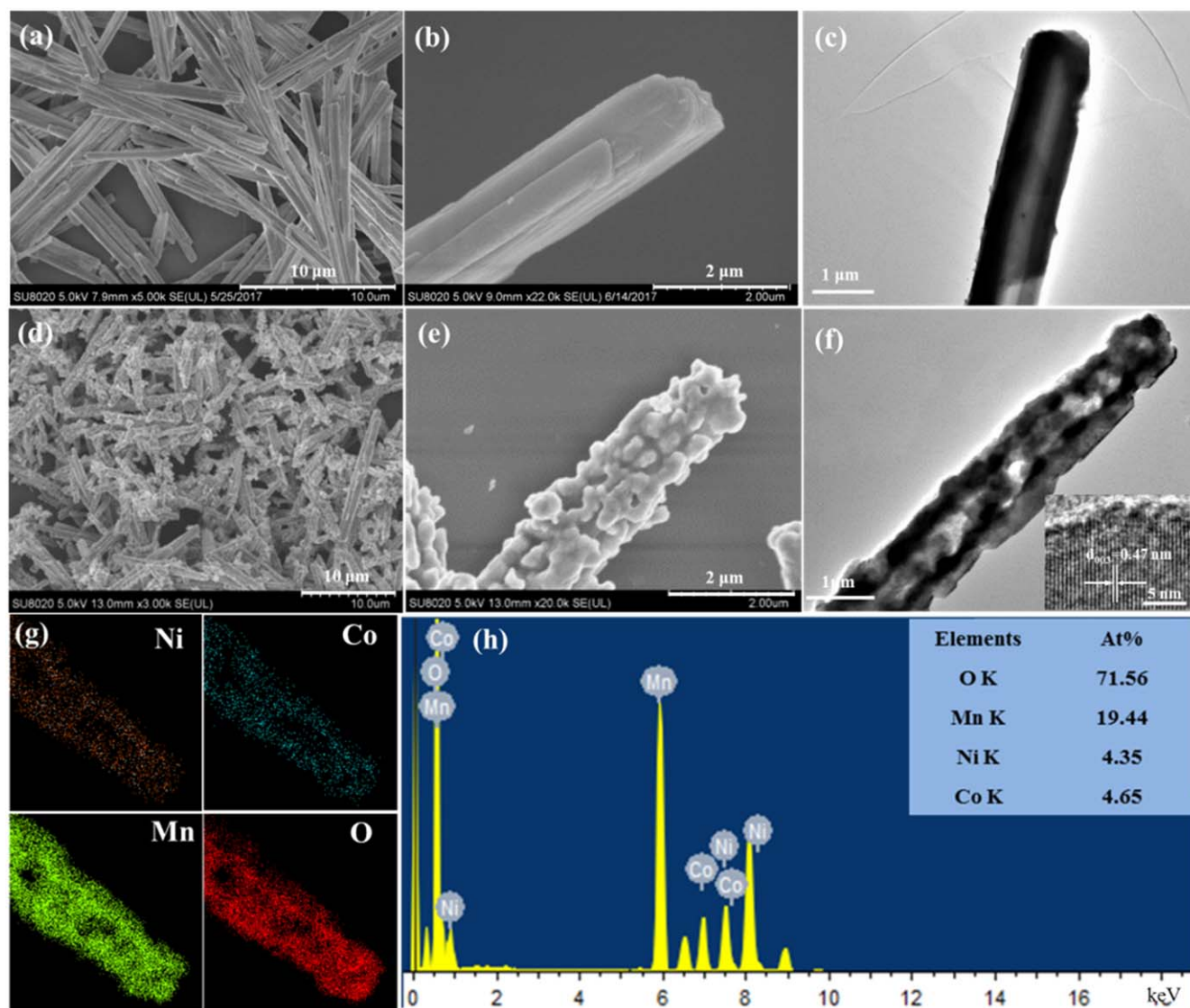
Figure 37. (a), (b), (d)–(e) FESEM images and (c), (f) TEM images for (a)–(c) the oxalate precursor and (d)–(f) $Li_{1.2}Ni_{0.13}Co_{0.13}Mn_{0.54}O_2$ microtubes; (g) elemental mappings and (h) EDS spectrum for a single $Li_{1.2}Ni_{0.13}Co_{0.13}Mn_{0.54}O_2$ microtube. Reproduced from [31] with permission from The Royal Society of Chemistry.

are assembled by nanosized particle building blocks in 100–300 nm, full of pores and voids [31].

The current sequential precipitation strategy to achieve the hollow structure of Li-rich layered oxides can be well integrated with the previous co-precipitation method mediated with the ethanol-water mixed solvent for the synthesis of $0.5Li_2MnO_3 \cdot 0.5LiNi_{1/3}Co_{1/3}Mn_{1/3}O_2$ solid microbars. As presented in figures 38(a) and (c), the sequential precipitation/mixed solvent coupled strategy offers the oxalate precursor of $MC_2O_4 \cdot xH_2O$ (M = Ni, Co and Mn) the long rod-shape morphology with the side in nearly squared shape and a hollow centered microstructure [31]. The elemental mappings and EDS spectrum suggest that each transition metal is uniformly distributed with the atomic ratio of Ni:Co:Mn = 1:1.4:4, close to that of the designed ratio (Ni:Co:Mn = 1:1:4) (figures 38(e), (f)). In contrast, the co-precipitation mediated by the mixed ethanol/water solvent only

produces the oxalate precursor in shorter and solid bar morphology.

The $Li_{1.2}Ni_{0.13}Co_{0.13}Mn_{0.54}O_2$ microtubes have shown good electrochemical properties. As presented in figure 29(b), the initial discharge capacity of the $Li_{1.2}Ni_{0.13}Co_{0.13}Mn_{0.54}O_2$ microtubes (denoted as LR-MTs) reaches 300 mAh g^{-1}, resulting in an initial coulombic efficiency of 86%, which is obviously improved in comparison with the particle-structured counterparts (82.6%). The LR-MTs sample delivers a good cycling performance with a high specific capacity of 210 mAh g^{-1} and the capacity retention of 91% at the rate of 0.5 C after 100 cycles (figure 29(d)). The minima in dQ/dV curves reveal a lower deviation from 3.8 V than these of $Li_{1.2}Ni_{0.13}Co_{0.13}Mn_{0.54}O_2$ nanoparticles, implying the reduced over potential for LR-MTs (figure 29(f)). The tubular and porous microstructures of $Li_{1.2}Ni_{0.13}Co_{0.13}Mn_{0.54}O_2$ hollow tubes are believed to be responsible for their good
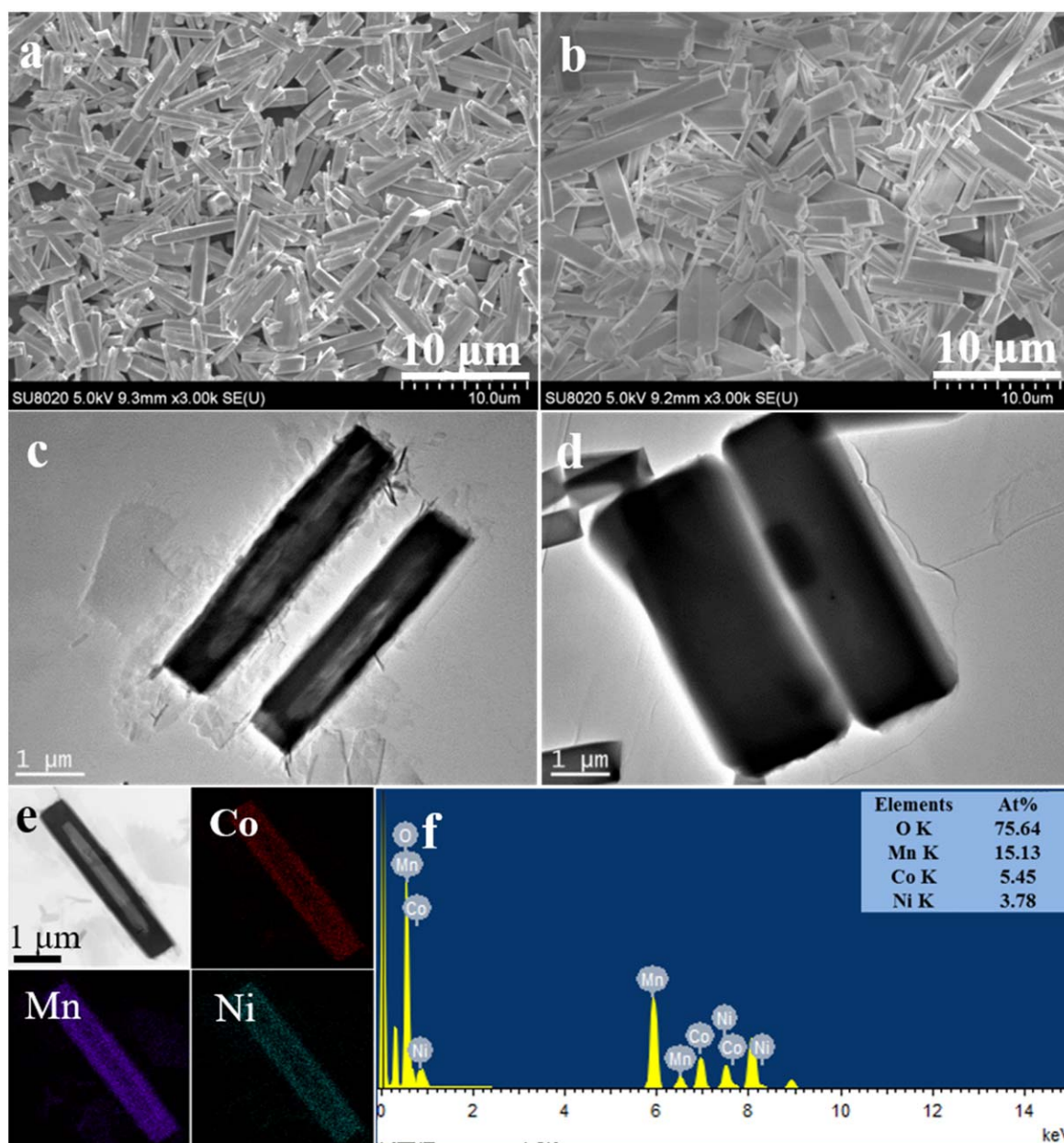
Figure 38. FESEM images and TEM images of $MC_2O_4 \cdot xH_2O$ (M = Ni, Co and Mn) precursor for Li-rich $Li_{1.2}Ni_{0.13}Co_{0.13}Mn_{0.54}O_2$ via (a), (c) sequential precipitation or (b), (d) co-precipitation; (e) elemental mappings and (f) EDS spectrum of $MC_2O_4 \cdot xH_2O$ (M = Ni, Co and Mn) precursor via sequential precipitation. Reproduced from [31] with permission from The Royal Society of Chemistry.

electrochemical performances, by offering an enhanced energy density for the higher output voltage, especially at the high discharge rate [31].

Our previous works have shown that both the oxalic acid and the reaction medium come into play on the morphology of the precursors that have the shapes of either long tubes or bars with solid or hollow interior. This of course determines the microstructure of the final electrode materials. The structural control of the precursors might be connected with the crystal growth habit of the different transition metal oxalates. Certain metal oxalate may prefer the growth along certain crystallographic directions under the help of surfactant as possibly played by the different solvents. This however requires further detailed studies.

2.4.3. $Li_{1.2}Ni_{0.13}Co_{0.13-x}Mn_{0.54}Al_xO_{2(1-y)}F_{2y}$ microspheres.

In addition to the previously proposed microstructural designs, doping by extrinsic defects is an alternative way capable of tuning the intrinsic chemistry of the cathode materials for improved electrochemical performances. The simplest example is the substitution of Co in $LiCoO_2$ to produce various derivatives of $LiNi_xCo_yMn_{1-x-y}O_2$, in the purposes of using high-lying Mn^{4+} e_g band to stabilize the structure and moderately high-lying Ni^{2+} e_g band to enhance the charge capacity, as introduced in section 2.3 [38].

Various cationic dopings have been exerted on Li-rich layerd oxide cathode materials, including Mg, Al, Co, Fe, Ru, Cr, etc. The incorporation of electrochemically inactive cations, such as Mg^{2+} and Al^{3+}, remarkably reduces the

Figure 39. Schematic diagram of the preparation of precursors $Ni_{0.13}Co_{0.13-x}Mn_{0.54}Al_x(CO_3)_{0.8+0.5x}$ and cathode materials $Li_{1.2}Ni_{0.13}Co_{0.13-x}Mn_{0.54}Al_xO_{2(1-y)}F_{2y}$ (LR-NCM). Reprinted from [10], Copyright 2017 with permission from Elsevier.

capacity induced by anionic redox (also called as sloping region or oxygen-loss plateau) but increases its structural stability due to its stronger interaction with the lattice oxygen. The substitution by the cations capable of being further oxidized above +4, e.g. Ru and Cr, significantly increase the length of the sloping region [2]. Anionic doping is often achieved via the substitution of O^{2-} by a small amount of F^-, which could slightly increase the lattice volume probably due to the partial reduction of the neighboring transition metal induced by the charge compensation of F^- [41, 42]. As a result, the rate capability can be improved. In addition, F doping could retard the layered-to-spinel phase transition, thus enhancing the capacity retention and stabilizing the discharge plateau.

The positive effect on electrodes varies from different dopants. However, mono-doping strategy could not effectively resist major drawbacks of Li-rich layered cathode materials, which brings our conceptual design that Al&F co-doping may be superior due to possible synergistic effect on the electrochemical performances of the $Li_{1.2}Ni_{0.13}Co_{0.13}Mn_{0.54}O_2$ lithium-rich layered cathode materials [10]. As illustrated in figure 39, the Al doping has been conducted in the co-precipitation process which accomplishes a uniform distribution in atomic scale. F is doped in the subsequent lithiation reaction for the precursor.

Compared to the hydroxide precursor, the Li-rich NCM samples (FESEM images shown in figure 40) present porous spherical morphology with the shrunken sizes of about 2.2 μm, due to the decomposition and sintering effect during calcination [10]. The microsized spheres are built by many primary nanoparticles. As compared in figure 40, the mono- or co-doping have no obvious effect on the size or morphology of the final products. The EDS spectrum and elemental mapping suggests the successful synthesis of the target F-&Al co-doped lithium-rich cathode materials with uniform elemental distributions.

The discharge/charge curves strongly suggest that the mono-doping by either Al or F can significantly improve the electrochemical performances, such as enhanced capacity retention and alleviated voltage decay. The capacity retentions are more than 88% for the doped cathodes, significantly higher than that of bare sample (~77%) after 150 cycles at 0.5 C (figures 41(a)–(e)). Moreover, the Al&F co-doped cathode material $Li_{1.2}Ni_{0.13}Co_{0.13-x}Mn_{0.54}Al_xO_{2(1-y)}F_{2y}$ ($x = 0.01$; $y = 0.03$) has further alleviated voltage decay (figure 41(d)). Especially, the difference is more pronounced after a longer electrochemical cycling (figure 41(f)).

Further electrochemical measurements reveal that the doped cathodes display enhanced rate capabilities than the bare sample, especially under the high current density of 10 C (figure 42(a)). The improvement should be attributed to the reduced resistance for electrons and lithium ions, as evidenced by the Nyquist plots obtained in electrochemical impedance spectrum (figure 42(b)). The thermal stability is a major concern of lithium-rich layered oxide cathode materials, due to the gradual evolution of oxygen-containing gaseous species especially under elevated temperature. The DSC curves for the doped $Li_{1.2}Ni_{0.13}Co_{0.13-x}Mn_{0.54}Al_xO_{2(1-y)}F_{2y}$ cathode after delithiation are given in figure 42(c). As presented in the plots, the exothermal peak of the doped samples are significantly shifted to higher temperature, with the lowered area beneath the peaks, implying the significantly reduced heat generation after doping. Especially, the Al&F co-doped cathode exhibits the exothermal peak at the highest temperature of 273 °C and lowest heat generation of 221 J g^{-1}, outstanding the mono-doped samples.

3. Conclusions and perspective

In this review, we mainly focus on the progress in LIB cathode materials made by our group, with the purpose of
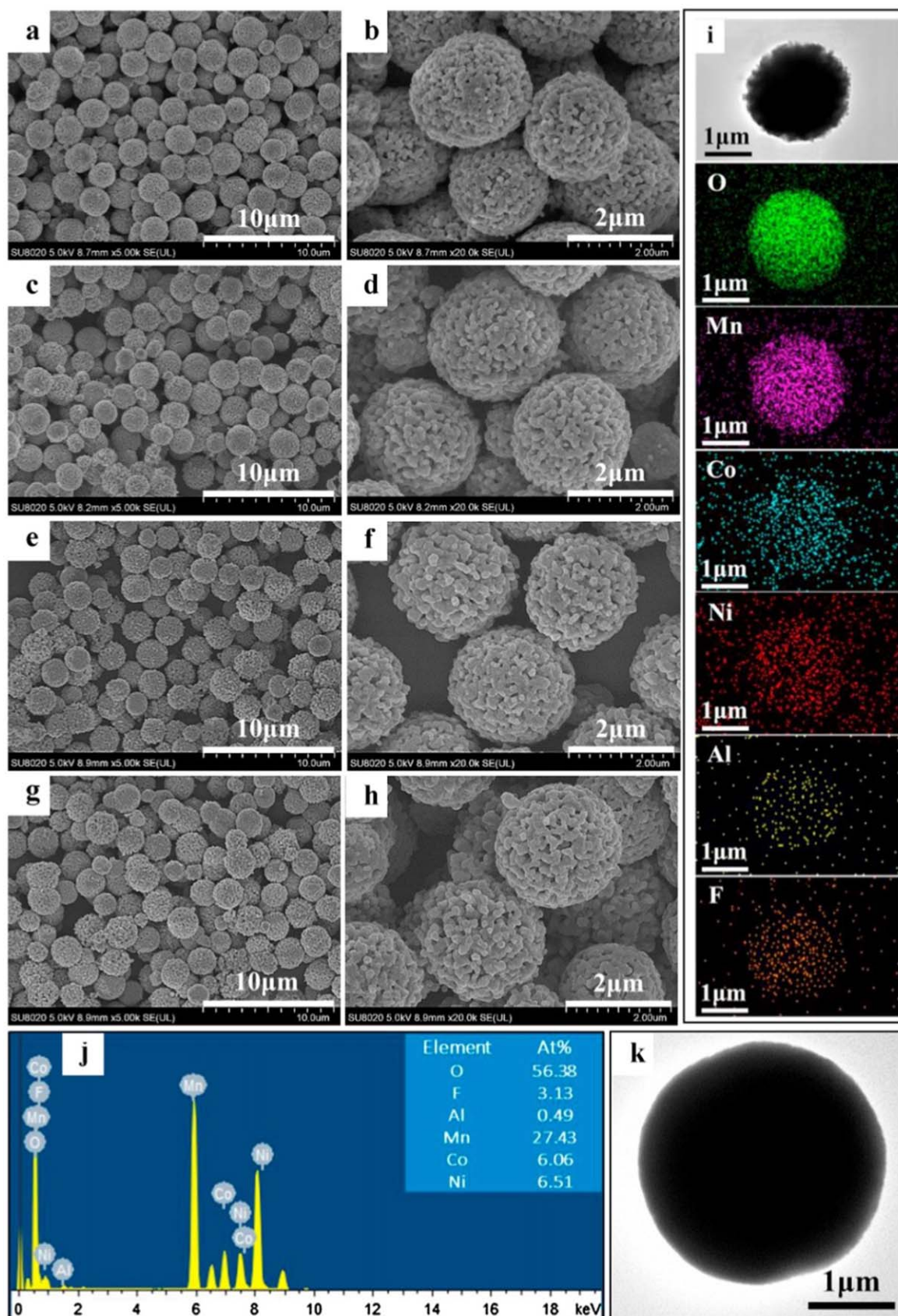
Figure 40. FESEM images of $Li_{1.2}Ni_{0.13}Co_{0.13-x}Mn_{0.54}Al_xO_{2(1-y)}F_{2y}$ for (a), (b) $x = 0$, $y = 0$; (c), (d) $x = 0.01$, $y = 0$; (e), (f) $x = 0$, $y = 0.03$; (g), (h) $x = 0.01$, $y = 0.03$; (i) elemental mappings and (j) EDS spectrum for $x = 0.01$ and $y = 0.03$; (k) TEM image of $Ni_{0.13}Co_{0.13}Mn_{0.54}(CO_3)_{0.8}$ (the precursor of the bare material). Reprinted from [10], Copyright 2017 with permission from Elsevier.
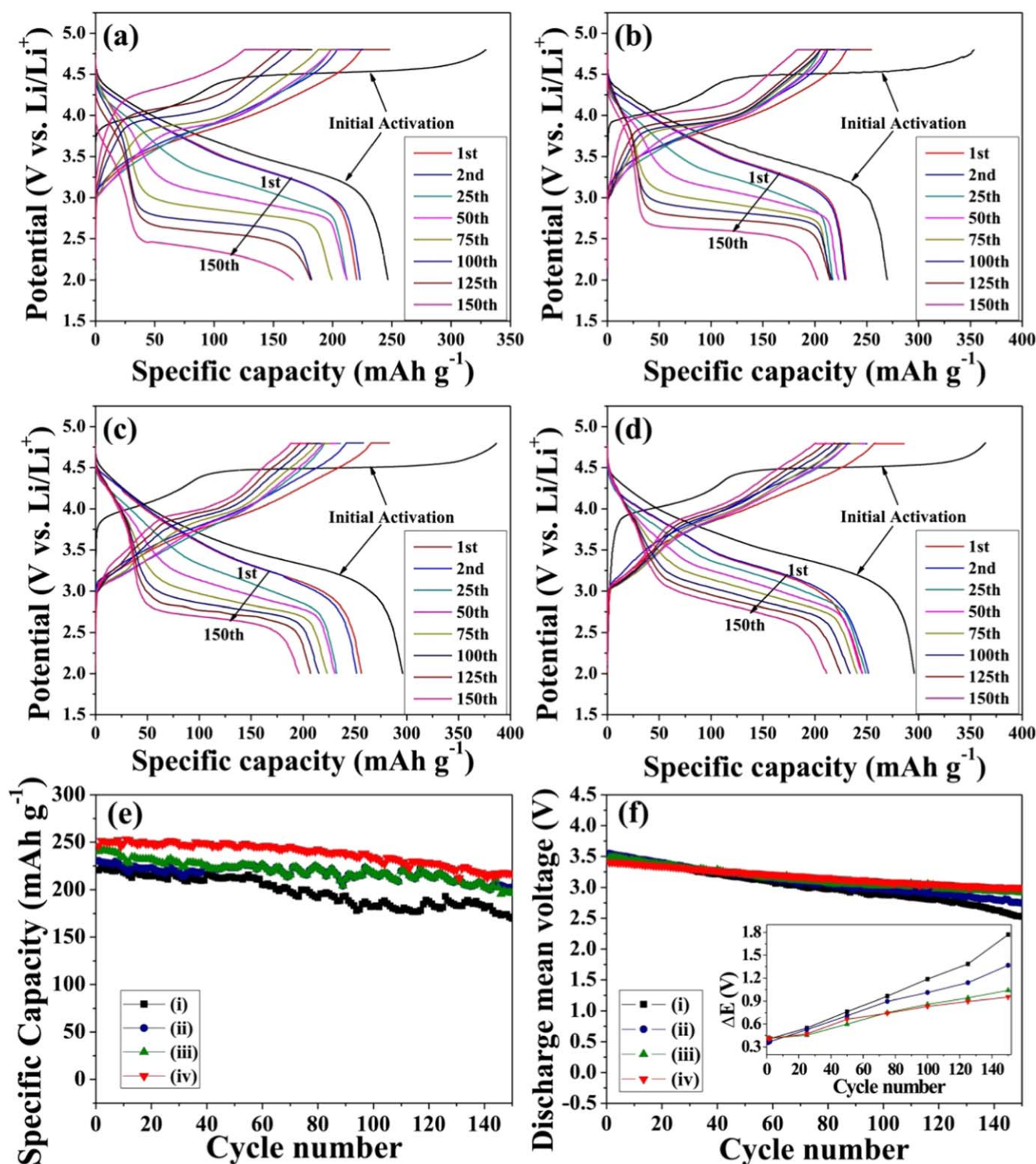
**Figure 41.** Charge–discharge profiles from galvanostatic cycling of $Li_{1.2}Ni_{0.13}Co_{0.13-x}Mn_{0.54}Al_xO_{2(1-y)}F_{2y}$ for (a) $x = 0$, $y = 0$; (b) $x = 0.01$, $y = 0$; (c) $x = 0$, $y = 0.03$; (d) $x = 0.01$, $y = 0.03$ at 0.5 C rate between 2.0 and 4.8 V after activation at 0.1 C for 3 cycles. (e) Galvanostatic cycle performance and (f) plots of the discharge mean potential versus cycle number: (i)–(iv) correspond with (a)–(d), respectively. The inset of (f) is plots of ΔE versus cycle number, where $\Delta E = E_c - E_d$, E_c is the charge mean voltage and E_d is the discharge mean voltage. Reprinted from [10], Copyright 2017 with permission from Elsevier.

fully exploring the potentials of materials' electrochemical properties by microstructural designs. We describe the crystal structures of four main cathode families of olivine $LiFePO_4$, spinel $LiMn_2O_4$, layered $LiMO_2$ and Li-rich layered $Li_{1+x}M_{1-x}O_2$ (M = Ni, Co, Mn). Through the examples we have explored, we can see that the microstructures play a pivotal role on the electrochemical performances of each specific cathode materials. For instance, by designing the 1D bar-like Li-rich $0.5Li_2MnO_3 \cdot 0.5LiNi_{1/3}Co_{1/3}Mn_{1/3}O_2$ materials of high porosity and structural integrity, we achieve
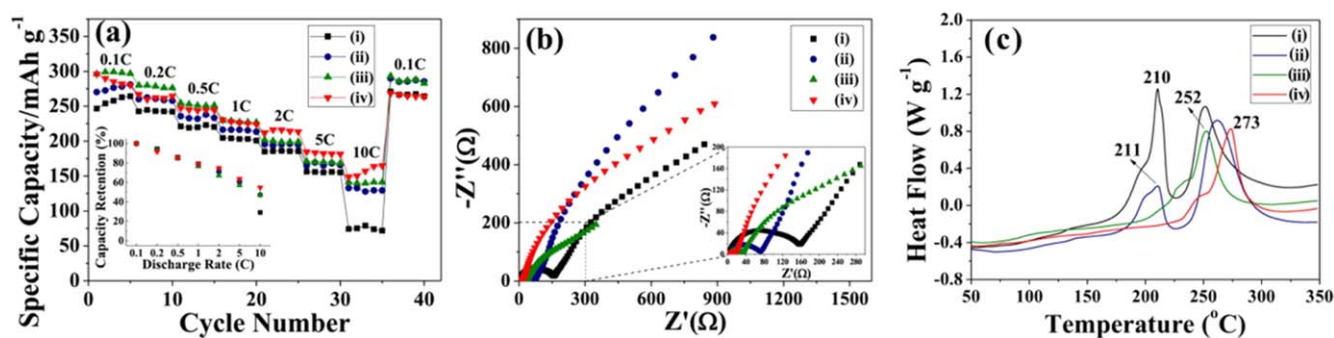
Figure 42. (a) Rate capability and (b) Nyquist plots of $Li_{1.2}Ni_{0.13}Co_{0.13-x}Mn_{0.54}Al_xO_{2(1-y)}F_{2y}$ and (c) DSC curves of the delithiated cathodes for: (i) $x = 0$, $y = 0$; (ii) $x = 0.01$, $y = 0$; (iii) $x = 0$, $y = 0.03$; (iv) $x = 0.01$, $y = 0.03$. The rate capability is conducted between 2.0 and 4.8 V. Coin cells with full charge status (to 4.8 V) after cycling at 0.1 C rate between 2.0 and 4.8 V are used for EIS. Reprinted from [10], Copyright 2017 with permission from Elsevier.

significantly increased electrochemical properties, including the higher discharge capacity and better cycling and rate capabilities. The structural design requires elegant manipulations of the nucleation and crystallization kinetics for the precursors and/or the final products, for which the factors capable of affecting the kinetics, e.g. the starting chemicals, reaction media and reaction sequences, should be selected purposely. We hope that this review can build a preliminary base on the microstructure-performance relationship for battery chemists.

It should be noted that some of the four cathode material categories, such as $LiFePO_4$ and $LiNi_{1/3}Co_{1/3}Mn_{1/3}O_2$, have been commercialized for the applications in electrical vehicles. Some are on the battery manufacture's near-future technology roadmap towards the automotive industry, including e.g. $LiNi_{0.5}Co_{0.2}Mn_{0.3}O_2$ and $LiNi_{0.6}Co_{0.2}Mn_{0.2}O_2$. Although Ni-rich and especially Li-rich layered oxides possess extremely high capacities, their large capacities are significantly traded off by their low cycling lives and major safety concerns. Their commercialization still requires much more research effort.

Modifications of these two material categories are indispensible to improve the cycling and safety performances, although the energy densities have to be sacrificed to some extent [43]. Multiple studies have proven that many irreversible structural changes occur on the top thin layer of the cathode particles during repeated charging/discharging cycles, including transition metal migration and phase transition. Therefore, functional coating is a simple but effective approach among different modification methods, which can enhance the rate performance due to the improved electrical and Li^+ conductivities, limit the capacity decay due to the suppressed side reactions between cathodes and electrolytes as well as suppress the thermal instability [2]. However, surface coating is not effective in mitigating the voltage decay of lithium-rich cathode materials, which may also occur in the bulk. Due to the structural similarity between Li_2MnO_3 phase and conventional layered oxides, it is of general difficulty to identify the local structural changes upon repeated runs. This hinders our substantial understanding of the cycling mechanism. It is thus more challenging to combat the issues of Li-rich layered cathode materials. Fortunately, we have seen many recent outstanding

research works have been done to mitigate their intrinsic issues. We could expect the near-future application of these advanced cathode materials to the commercial level.

Acknowledgments

ORCID iDs

Weixin Zhang ⓘ https://orcid.org/0000-0001-6979-8901

References

[1] Xu B, Qian D N, Wang Z Y and Meng Y S 2012 Recent progress in cathode materials research for advanced lithium ion batteries *Mater. Sci. Eng.* R **73** 51–65

[2] Manthiram A, Knight J C, Myung S T, Oh S M and Sun Y K 2016 Nickel-rich and lithium-rich layered oxide cathodes: progress and perspectives *Adv. Energy Mater.* **6** 1501010

[3] Xu J, Lin F, Doeff M M and Tong W 2017 A review of Ni-based layered oxides for rechargeable Li-ion batteries *J. Mater. Chem.* **5** 874–901

[4] Li M, Lu J, Chen Z W and Amine K 2018 30 years of lithium-ion batteries *Adv. Mater.* **30** 1800561

[5] Mizushima K, Jones P C, Wiseman P J and Goodenough J B 1980 Li_xCoO_2 ($0 < x \leqslant 1$): a new cathode material for batteries of high energy density *Mater. Res. Bull.* **15** 783–9

[6] Hu M, Pang X L and Zhou Z 2013 Recent progress in high-voltage lithium ion batteries *J. Power Sources* **237** 229–42

[7] Liu W, Oh P, Liu X E, Lee M J, Cho W, Chae S, Kim Y and Cho J 2015 Nickel-rich layered lithium transition-metal oxide for high-energy lithium-ion batteries *Angew. Chem. Int. Ed.* **54** 4440–57

[8] Li S, Ma G, Guo B, Yang Z H, Fan X M, Chen Z X and Zhang W X 2016 Kinetically controlled synthesis of LiNi$_{0.5}$Mn$_{1.5}$O$_4$ micro- and nanostructured hollow spheres as high-rate cathode materials for lithium ion batteries *Ind. Eng. Chem. Res.* **55** 9352–61

[9] Tang W J, Chen Z X, Xiong F, Chen F, Huang C, Gao Q, Wang T Z, Yang Z H and Zhang W X 2019 An effective etching-induced coating strategy to shield LiNi$_{0.8}$Co$_{0.1}$Mn$_{0.1}$O$_2$ electrode materials by LiAlO$_2$ *J. Power Sources* **412** 246–54

[10] Guo B, Zhao J H, Fan X M, Zhang W, Li S, Yang Z H, Chen Z X and Zhang W X 2017 Aluminum and fluorine co-doping for promotion of stability and safety of lithium-rich layered cathode material *Electrochim. Acta* **236** 171–9

[11] Xiao J, Zheng J M, Li X L, Shao Y Y and Zhang J G 2013 Hierarchically structured materials for lithium batteries *Nanotechnology* **24** 424004

[12] Vu A, Qian Y Q and Stein A 2012 Porous electrode materials for lithium-ion batteries-How to prepare them and what makes them special *Adv. Energy Mater.* **2** 1056–85

[13] Wei G Z, Lu X, Ke F S, Huang L, Li J T, Wang Z X, Zhou Z Y and Sun S G 2010 Crystal habit-tuned nanoplate material of Li[Li$_{1/3-2x/3}$Ni$_x$Mn$_{2/3-x/3}$]O$_2$ for high-rate performance lithium-ion batteries *Adv. Mater.* **22** 4364–7

[14] Padhi A K, Nanjundaswamy K S, Masquelier C, Okada S and Goodenough J B 1997 Effect of structure on the Fe^{3+}/Fe^{2+} redox couple in iron phosphates *J. Electrochem. Soc.* **144** 1609–13

[15] Pei B, Yao H X, Zhang W X and Yang Z H 2012 Hydrothermal synthesis of morphology-controlled LiFePO$_4$ cathode material for lithium-ion batteries *J. Power Sources* **220** 317–23

[16] Peng L L, Zhang X, Fang Z W, Zhu Y, Xie Y J, Cha J J and Yu G H 2017 General facet-controlled synthesis of single-crystalline {010}-oriented LiMPO$_4$ (M = Mn, Fe, Co) nanosheets *Chem. Mater.* **29** 10526–33

[17] Zaghib K, Mauger A, Goodenough J B, Gendron F and Julien C M 2007 Electronic, optical, and magnetic properties of LiFePO$_4$: small magnetic polaron effects *Chem. Mater.* **19** 3740–7

[18] Wang Q, Zhang W X, Yang Z H, Weng S Y and Jin Z J 2011 Solvothermal synthesis of hierarchical LiFePO$_4$ microflowers as cathode materials for lithium ion batteries *J. Power Sources* **196** 10176–82

[19] Zhang J, Lu J B, Bian D C, Yang Z H, Wu Q and Zhang W X 2014 Solvothermal synthesis of hierarchical LiFePO$_4$ microplates with exposed (010) faces as cathode materials for lithium ion batteries *Ind. Eng. Chem. Res.* **53** 12209–15

[20] Park O K, Cho Y, Lee S, Yoo H C, Song H K and Cho J 2011 Who will drive electric vehicles, olivine or spinel? *Energy Environ. Sci.* **4** 1621–33

[21] Lee E and Persson K A 2013 First-principles study of the nano-scaling effect on the electrochemical behavior in LiNi$_{0.5}$Mn$_{1.5}$O$_4$ *Nanotechnology* **24** 424007

[22] Wang Q, Zhang W X and Yang Z H unpublished work

[23] Liu W, Farrington G C, Chaput F and Dunn B 1996 Synthesis and electrochemical studies of spinel phase LiMn$_2$O$_4$ cathode materials prepared by the Pechini process *J. Electrochem. Soc.* **143** 879–84

[24] Liu D *et al* 2012 Synthesis of pure phase disordered LiMn$_{1.45}$Cr$_{0.1}$Ni$_{0.45}$O$_4$ by a post-annealing method *J. Power Sources* **217** 400–6

[25] Liu Z L, Yu A S and Lee J Y 1999 Synthesis and characterization of LiNi$_{1-x-y}$Co$_x$Mn$_y$O$_2$ as the cathode materials of secondary lithium batteries *J. Power Sources* **81-82** 416–9

[26] Cui S H *et al* 2016 Optimized temperature effect of Li-ion diffusion with layer distance in Li(Ni$_x$Mn$_y$Co$_z$)O$_2$ cathode materials for high performance Li-ion battery *Adv. Energy Mater.* **6** 1501309

[27] Manthiram A, Vadivel Murugan A, Sarkar A and Muraliganth T 2008 Nanostructured electrode materials for electrochemical energy storage and conversion *Energy Environ. Sci.* **1** 621–38

[28] MacNeil D D, Lu Z and Dahn J R 2002 Structure and Electrochemistry of Li[Ni$_x$Co$_{1-2x}$Mn$_x$]O$_2$ (0 ⩽ 1 ⩽ /2) *J. Electrochem. Soc.* **149** A1332–6

[29] Yang Z H, Lu J B, Bian D C, Zhang W X, Yang X N, Xia J F, Chen G D, Gu H Y and Ma G 2014 Stepwise co-precipitation to synthesize LiNi$_{1/3}$Co$_{1/3}$Mn$_{1/3}$O$_2$ one-dimensional hierarchical structure for lithium ion batteries *J. Power Sources* **272** 144–51

[30] Xia Q, Zhao J H, Wang K, Li S, Guo B, Tian Y, Yang Z H and Zhang W X 2017 Synthesis and characterization of LiNi$_{0.5}$Co$_{0.2}$Mn$_{0.3}$O$_2$ cathode materials by stepwise co-precipitation *CIESC J.* **68** 1239–46

[31] Chen F, Zhang W X, Fu J R, Yang Z H, Fan X M, Zhang W B, Chen Z X, Huang M Q and Yang S H 2018 Sequential precipitation induced interdiffusion: a general strategy to synthesize microtubular materials for high performance lithium ion battery electrodes *J. Mater. Chem.* A **6** 18430–7

[32] Liu J and Sun X L 2014 Elegant design of electrode and electrode/electrolyte interface in lithium-ion batteries by atomic layer deposition *Nanotechnology* **26** 024001

[33] Rossouw M H, Liles D C and Thackeray M M 1993 Synthesis and structural characterization of a novel layered lithium manganese oxide, Li$_{0.36}$Mn$_{0.91}$O$_2$, and its lithiated derivative, Li$_{1.09}$Mn$_{0.91}$O$_2$ *J. Solid State Chem.* **104** 464–6

[34] Nayak P K, Erickson E M, Schipper F, Penki T R, Munichandraiah N, Adelhelm P, Sclar H, Amalraj F, Markovsky B and Aurbach D 2018 Review on challenges and recent advances in the electrochemical performance of high capacity Li- and Mn-rich cathode materials for Li-ion batteries *Adv. Energy Mater.* **8** 1702397

[35] Zheng J M, Myeong S, Cho W, Yan P F, Xiao J, Wang C M, Cho J and Zhang J G 2017 Li- and Mn-rich cathode materials: challenges to commercialization *Adv. Energy Mater.* **7** 1601284

[36] Yu H J, Ishikawa R, So Y G, Shibata N, Kudo T, Zhou H S and Ikuhara Y 2013 Direct atomic-resolution observation of two phases in the Li$_{1.2}$Mn$_{0.567}$Ni$_{0.166}$Co$_{0.067}$O$_2$ cathode material for lithium-ion batteries *Angew. Chem. Int. Ed.* **52** 5969–73

[37] Yu X Q, Hu E Y, Bak S, Zhou Y N and Yang X Q 2016 Strategies to curb structural changes of lithium/transition metal oxide cathode materials & the changes' effects on thermal & cycling stability *Chin. Phys.* B **25** 018205

[38] Assat G and Tarascon J M 2018 Fundamental understanding and practical challenges of anionic redox activity in Li-ion batteries *Nat. Energy* **3** 373–86

[39] Li B and Xia D G 2017 Anionic redox in rechargeable lithium batteries *Adv. Mater.* **29** 1701054

[40] Ma G *et al* 2016 A general and mild approach to controllable preparation of manganese-based micro- and nanostructured bars for high performance lithium-ion batteries *Angew. Chem. Int. Ed.* **55** 3667–71

[41] Li L, Song B H, Chang Y L, Xia H, Yang J R, Lee K S and Lu L 2015 Retarded phase transition by fluorine doping in Li-rich layered Li$_{1.2}$Mn$_{0.54}$Co$_{0.13}$O$_2$ cathode material *J. Power Sources* **283** 162–70

[42] Wu Y and Manthiram A 2007 Effect of Al^{3+} and F$^-$ doping on the irreversible oxygen loss from layered Li[Li$_{0.17}$Mn$_{0.58}$Ni$_{0.25}$]O$_2$ cathodes *Electrochem. Solid-State Lett.* **10** A151–4

[43] Myung S T, Maglia F, Park K J, Yoon C S, Lamp P, Kim S J and Sun Y K 2017 Nickel-rich layered cathode materials for automotive lithium-ion batteries: achievements and perspectives *ACS Energy Lett.* **2** 196–223